Aerodynamic Optimization of a Flying V Aircraft using a Vortex Lattice Method

Francesco Granata

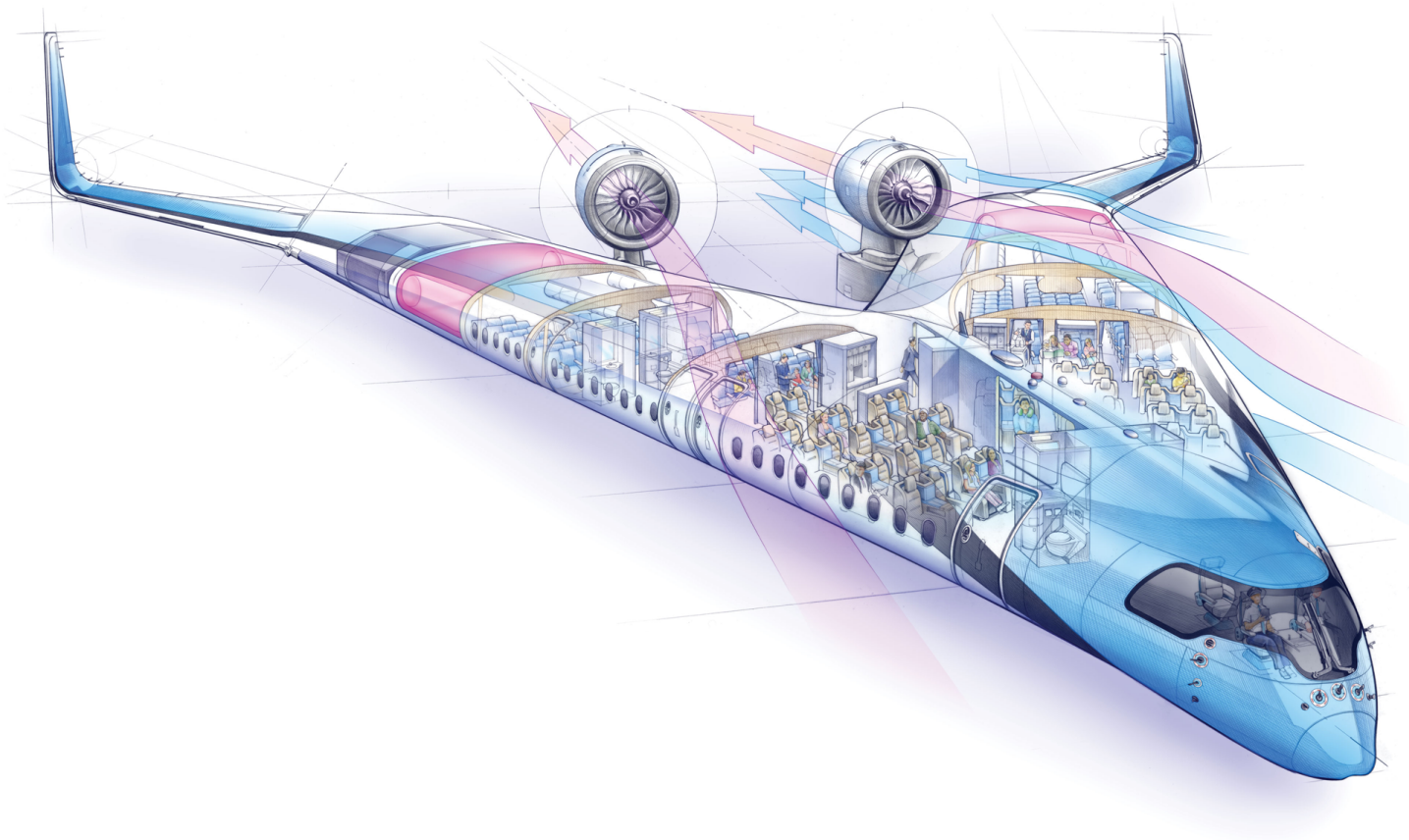

TU Delft

Aerodynamic Optimization of a Flying V Aircraft using a Vortex Lattice Method

Master Thesis

Faculty of Aerospace Engineering

Flight Performance

Student:

Francesco Granata

5394570

Thesis Committee:

Dr.Ir.	Roelof Vos (chair)
Dr.Ing.	Justus Benad (supervisor)
Prof.	Marios Kotsonis
Dr.Ir.	Maurice Hoogreef

Institution: Delft University of Technology

Cover: https://www.nationalgeographic.com/magazine/graphics/take-a-look-inside-the-flying-v-feature by Bruce Morser

TU Delft Delft University of Technology

Preface

The work presented in this document marks the end of a long academic journey. None of this would have been possible without the loving support of many people around me.

First and foremost, I extend my heartfelt gratitude to Nonno Giovanni, who I have been privileged to have by my side and with whom I would have loved sharing this work. To my beloved mother, Debora, you have been a constant loving presence throughout my life, enabling me to explore new horizons even when we were separated by distance. I can never express enough appreciation for all that you have done and continue to do for me. My thoughts also turn to my father, Sergio, whose enduring values and invaluable life lessons will forever reside in my heart.

I am indebted to my Moai friends and to Daniele, who daily remind me that our bond transcends those of a simple friendship. A resounding shout-out goes to the Jaagpad crew, Bernardo, Matteo, Blas, Marinos, and Rodrigo, who have never been mere roommates but life companions with whom I've shared countless days under one roof.

Thanks to Julia, who deserves special mention for her unwavering support, love, and patience over the past two years, guiding me through the most challenging moments with unyielding dedication.

Last but certainly not least, I would like to express my gratitude to Justus for giving me the opportunity to work on this motivating project. His patient supervision and guidance throughout the entirety of the project have been instrumental in steering me toward the successful completion of this endeavor.

Delft, September 2023

"Non est ad astra mollis e terris via."

L. A. Seneca

Summary

To address the environmental impact of air travel, the industry has introduced various solutions, including sustainable fuels and new aircraft configurations. The Flying V is one such concept that promises a 20% reduction in fuel consumption compared to its most advanced competitor. Unlike traditional commercial airplanes, the Flying V is a tailless flying-wing design without a tubular fuselage, horizontal, and vertical tailplane, using elevons and winglets featuring rudders for control. This study aimed to optimize the wing geometry of the Flying V aircraft to minimize induced drag under specific subsonic conditions ($M = 0.6$) and a given lift coefficient of 0.26. The approach combined a Vortex Lattice Method (VLM) with an optimization algorithm, specifically using the Athena Vortex Lattice (AVL) software for aerodynamics calculations. A low-fidelity method, such as a VLM, allows a faster and deeper exploration of the design space than a high-fidelity method like Computational Fluid Dynamics (CFD). To improve the Flying V's design, a simpler parameterization was introduced to represent the complex model of the Outer Mold Line (OML) of the aircraft. It involved eight sections along half the wingspan. The inboard wing sections were parameterized in a wire-frame style, with the front part representing the location of the passengers' cabin, requiring fixed dimensions and inclination to accommodate a suitable cabin floor. The other sections' geometry was mainly described by the total inclination angle. The design vector included the aft angles of the first three sections, the total incidence angle of the last four sections, and the dihedral of the outboard wing, which is useful to ensure a straight hinge line for control power. A total of 8 design variables were utilized during the optimization process. Two aerodynamic constraints were implemented to ensure feasible optimized results. The first constraint was related to the resulting angle of attack computed by AVL based on the defined geometry and lift coefficient input. Such constraint was necessary to control the total inclination of the passengers' cabin during cruise. The second constraint required a positive distance between the aircraft's neutral point and the center of pressure, with a minimum value of 2% of the Mean Aerodynamic Chord, serving as a measure of the aircraft's static margin. In addition, a simplified empirical viscous module was introduced to get a better estimation of the total lift-to-drag ratio. The final design showed a 4.38% increase in lift-to-drag ratio compared to the initial design and a 10.5% reduction in induced drag coefficient. Furthermore, the optimized lift distribution showed an averaged elliptical shape with respect to the initial design. This showcases the significant enhancements achieved in the aerodynamic performance of the optimized configuration.

Contents

List of Figures

List of Tables

Nomenclature

Abbreviations

Abbreviation	Definition
AVL	Athena Vortex Lattice
CAD	Computer-Aided Design
CFD	Computational Fluid Dynamics
COBYLA	Constrained Optimization by Linear Approximation
OML	Outer Mould Line
VLM	Vortex Lattice Method

Symbols

Symbol	Definition	Unit
AR	Aspect Ratio	$[-]$
a_i	Section 'i' incidence angle	$[^\circ]$
$a_{i,\text{aft}}$	Section 'i' aft part incidence angle	$[^\circ]$
$a_{i,\text{front}}$	Section 'i' front part incidence angle	$[^\circ]$
b	Semi wing-span	$[m]$
$\bar{c}$	Mean aerodynamic chord	$[m]$
c	Chord	$[m]$
C_{D_i}	Induced drag coefficient	$[-]$
C_{d_i}	Sectional induced drag coefficient	$[-]$
C_{D_v}	Viscous drag coefficient	$[-]$
C_F	Flat plate skin friction coefficient	$[-]$
C_ℓ	Sectional lift coefficient	$[-]$
C_L	Lift coefficient	$[-]$
C_m	Pitching moment coefficient	$[-]$
C_p	Pressure coefficient	$[-]$
D_i	Induced drag	$[N]$
d_i	Induced drag force per section	$[N/m]$
EE	Elementary Effect	$[-]$

Symbol	Definition	Unit
f	Form factor	$[-]$
$\bar{g}$	Constraints Vector	$[-]$
L	Lift force	$[N]$
LE_i	Section 'i' Leading Edge	$[m]$
ℓ	Lift force per section	$[N/m]$
M	Mach Number	$[-]$
PG	Prandtl-Glauert factor	$[-]$
q_∞	Dynamic pressure	$[kg/(m \cdot s^2)]$
Re	Reynolds number	$[-]$
S	Wing (reference) area	$[m^2]$
S_{wet}	Wetted area	$[m^2]$
TE_i	Section 'i' Trailing Edge	$[m]$
u	Velocity X component	$[m/s]$
u'	Velocity perturbation - X component	$[m/s]$
V_∞	Freestream velocity	$[m/s]$
v	Velocity Y component	$[m/s]$
v'	Velocity perturbation - Y component	$[m/s]$
w	Velocity Z component - Downwash	$[m/s]$
w'	Velocity perturbation - Z component	$[m/s]$
X_{CP}	Center of pressure X location	$[m]$
X_{NP}	Neutral point X location	$[m]$
y	Spanwise coordinate	$[m]$
$\bar{y}$	Design Vector	$[-]$
α	Angle of attack	$[^\circ]$
α_i	Induced angle of attack	$[^\circ]$
α_{eff}	Effective angle of attack	$[^\circ]$
α_{value}	Angle of attack constraint value	$[^\circ]$
Γ	Outboard wing dihedral	$[^\circ]$
μ	Mean	$[-]$
μ^*	Normalized mean	$[-]$
ρ	Density	$[kg/m^3]$
σ	Standard deviation	$[-]$

1

Introduction

The aviation industry has been steadily growing since the 1970s, a trend which is expected to continue over the coming decades [1]. Such expansion necessitates a drastic response in order to limit the environmental impact of air travel. This is also required to meet the United Nations' 2030 sustainability goals [2]. For this purpose, industry and academic research have introduced a variety of solutions, ranging from alternative sustainable fuels to entirely new aircraft configurations [3]. The necessity to introduce the latter is a consequence of the plateau in the overall efficiency improvement curve reached with the advent of the Airbus A350 and the Boeing 787 latest versions [4]. Indeed, these aircraft currently represent the most advanced tube-and-wing configuration applications.

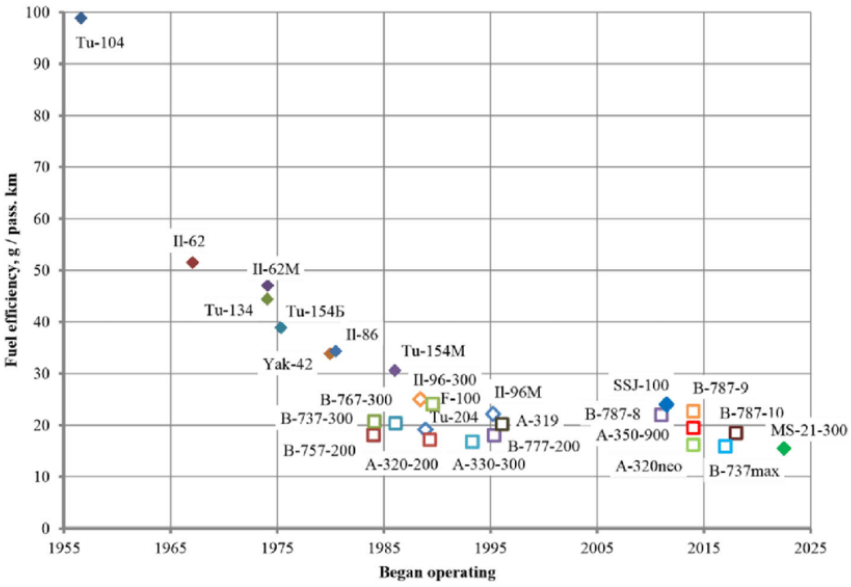

Figure 1.1: Aircraft fuel efficiency historical development [5].

The Flying V, proposed by J. Benad in 2015 [6], is a novel aircraft concept that promises to cut fuel consumption by 20% compared to the A350-900, Airbus' most advanced aircraft. The overall design of the Flying V differs significantly from that of typical commercial airplanes, as illustrated in Figure 1.2. It is a tailless flying-wing that lacks a tubular fuselage as well as a horizontal and vertical tailplane. Trailing-edge elevons are used mainly for achieving longitudinal and lateral control, while directional control is mainly provided through the use of winglets, featuring rudders. Many academic studies on the Flying V have been conducted lately, ranging from shape optimization studies to wind tunnel experiments and handling qualities investigation [4, 6–9]. In general, previous research agrees on the feasibility of the Flying V and on the benefits its design would bring.

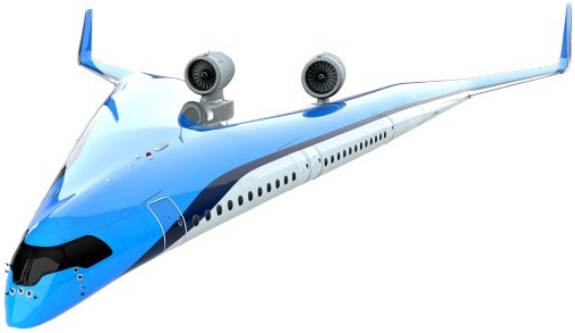

Figure 1.2: Flying V rendering.

1.1 Motivation & Problem Statement

In order to develop an accurate representation of the Outer Mould Line (OML) for the Flying V aircraft, the current design and parameterization were utilized to construct a detailed Computer-Aided Design (CAD) model. However, further design improvements require an aerodynamic optimization of the OML shape, specifically focusing on enhancing the lift distribution and reducing induced drag at cruise lift coefficient. Since the Flying V operates within the transonic regime, an optimization process utilizing high-fidelity techniques like Computational Fluid Dynamics (CFD) becomes necessary. However, due to the significant computational and time requirements associated with CFD, an initial optimization step employing a low-fidelity method is necessary to provide a preliminary design for the subsequent high-fidelity process. That introduces various aspects that need to be addressed. These include constructing a simplified parameterized model of the Flying V, which will be utilized in the optimization process calculations. Additionally, it is necessary to explore and assess the capabilities of a suitable low-fidelity method, in particular of a Vortex Lattice Method (VLM), that can ensure reliable aerodynamic calculations. Furthermore, attention must be given to specifying the geometric and aerodynamic constraints that are relevant when optimizing the overall design. It is possible to summarize the main objectives of the present research as follows:

"to optimize the wing geometry of the Flying V for minimum induced drag at a given lift coefficient in specific subsonic conditions by means of a VLM coupled with an optimization algorithm."

The research objective can be expanded into a broader question, the answer to which is the project's completion goal. It can be viewed as a lighthouse guiding the research that must be accomplished one small step at a time. The following is the research question:

"What is the minimum induced drag of the Flying V aircraft at a given lift coefficient in subsonic cruise conditions?"

Even though such a question embodies the aforementioned research objective, it is still quite broad and difficult to answer all at once. As a result, it is necessary to divide it into several sub-questions. When the answers to those questions are combined, they will provide a comprehensive and thorough solution to the main one.

- What parametric model best suits the optimization problem at hand?
- What are the geometrical and aerodynamics constraints to take into account?
- What are the capabilities of the VLM used to perform the aerodynamics analysis?
- What parameters have the most relevance for the analysis and how do they relate to the objective function?
- How accurately can the current Flying V model be adapted to the simplified and optimized parametric model?

1.2 Thesis Outline

The research structure is presented as follows: Chapter 2 focuses on the theoretical background necessary to address the thesis topic as well as on a brief overview of previous Flying V related studies; the methodology used to achieve the research goal is described in detail in Chapter 3 where the parametric model, the VLM chosen for aerodynamics calculations, and the structure of the optimization problem and algorithm are presented; Chapter 4 shows the validation of the VLM used; the results obtained are described and discussed in Chapter 5; finally, the conclusions of the research project and the recommendations for future work are presented in Chapter 6 and Chapter 7.

2

Background

This chapter is dedicated to equipping the reader with the essential theoretical foundation to accomplish the research objective stated earlier. Initially, a concise summary of previous studies concerning the Flying V is provided, outlining the path that has led to the current status of the project. Subsequently, key concepts in aerodynamics are introduced, specifically focusing on induced drag and its computation using Prandtl's lifting line theory, Trefftz plane analysis, and the Vortex Lattice Method. This sets the stage for the final section of the chapter, which presents the Athena Vortex Lattice software.

2.1 Flying V Background

The geometry of the Flying V wing was optimized in 2017 by F. Faggiano using both Computational Fluid Dynamics (CFD) and Vortex Lattice Method (VLM). A 25% increase in aerodynamic efficiency compared to the NASA Common Research Model was obtained [4]. The wing was swept back from 15° to 30°, Figure 2.1a and the outer wing was twisted down due to excessive loading in that region which resulted in a strong shock [4]. Moreover, the cabin structure was modified from two cylindrical sections to a single elliptical one, Figure 2.1b [4]. M. Hillen updated the parameterization of the Flying V geometry in 2020 to consider structural and manufacturing constraints, while also ensuring its suitability for use in an aerodynamic optimization routine [10]. A decrease of 15% was noticed in aerodynamic efficiency at cruise conditions with such a parameterization. The resulting aerodynamic shape of the Flying V showed certain shortcomings, which were first addressed in [11] with the aim of further increasing the overall aerodynamic efficiency. In 2022, a novel parameterization of the Flying V was introduced by Benad aimed at resolving these aerodynamic challenges. Central to the updated

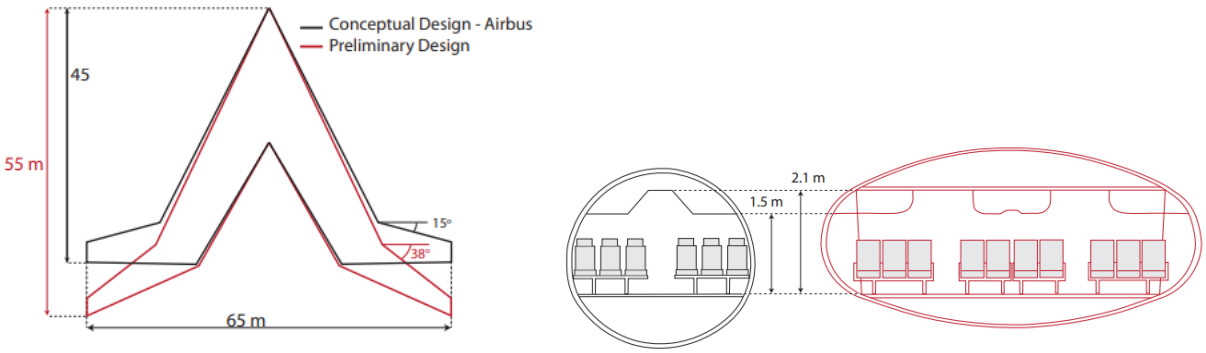

(a) Faggiano's resulting swept-back outer wing [4].

(b) Faggiano's resulting oval shaped fuselage [4].

Figure 2.1: Main design results obtained by Faggiano [4].

design is the introduction of an oval retention parameter in the transition wing section of the Flying V, which is described in detail in [12]. This parameterization is the baseline design used in the present study.

2.2 Induced Drag

The induced drag (D_i) is a drag component that is directly related to the vortices produced and shed downstream by a lifting surface. The induced drag can be introduced as follows according to J. Anderson [13]. The vortices at the wing tips induce a downward velocity in the region surrounding the wing. Such velocity component is called downwash and it is indicated with the symbol w. The combination of this downward velocity with the freestream velocity affects the local relative wind direction in proximity of each wing section. An illustration of this phenomenon is shown in Figure 2.2 below.

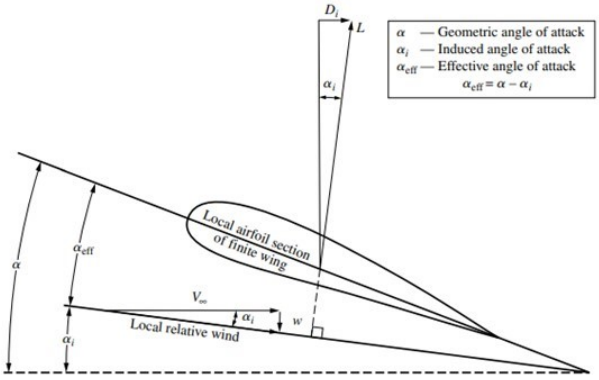

Figure 2.2: Illustration of induced drag origin [13].

As a result, the angle of attack that each airfoil along the wing experiences is the one between the chord line and the local relative wind, and it is defined as effective angle of attack. This is smaller than the geometric angle of attack at which the wing is at. The angle between the local relative wind, inclined downwards due to the downwash component, and the freestream velocity is referred to as the induced angle of attack (α_i). In symbols:

$$\alpha_{\text{eff}} = \alpha - \alpha_i \tag{2.1}$$

The inclination of the local relative wind is reflected on the direction of the lift vector which is perpendicular to it by definition. Being the lift vector tilted with respect to the direction normal to the freestream velocity, a lift component can be observed to be present in the freestream direction itself. Such a component is the induced drag D_i. Its origin is therefore to be found in the presence of the wing-induced downwash in the flow which is in turn directly related to the generation of lift.

2.3 Prandtl's Lifting Line Theory

The lifting line theory was presented by Prandtl to predict the aerodynamic characteristics of a finite wing, including induced drag. Such method can eventually be applied to wings with twist, different airfoils, and varying chords along the span but not to wings with dihedral or sweep [14]. The concept behind such theory is to represent the wing with a series of vortices placed on a line along the span of the wing itself. For each of these vortex, two vortex filaments expand infinitely downstream because a vortex filament cannot end in a fluid according to Helmoltzs theorem [15]. This vortex system is therefore called the horseshoe vortex because of its shape. In case an infinite number of vortices with strength $d\Gamma$ is assumed to be present along the lifting line, a distribution of $\Gamma(y)$ is obtained. This is sketched in the figure below where y_0 is an arbitrary location along the span, y is the coordinate in the span direction, and x the one in the freestream direction.

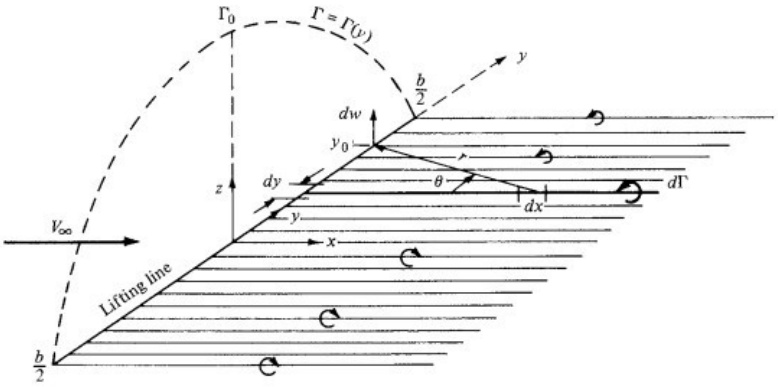

Figure 2.3: Illustration of horseshoe vortices along the lifting line [13].

The total downwash at each arbitrary location y_0 can be obtained by summing the contribution of each vortex on that point, which can be calculated with Biot-Savart law. The resulting expression is:

$$w\left(y_0\right) = -\frac{1}{4\pi}\int_{-b/2}^{b/2}\frac{(d\Gamma/dy)dy}{y_0 - y} \tag{2.2}$$

Reworking the angles of attack previously defined (assuming $C_{L_\alpha} = 2\pi$) and considering Kutta-Jukowski theorem, it is possible to get to the fundamental equation of Prandtls lifting-line theory (please refer to [13] for further derivations):

$$\alpha\left(y_0\right) = \frac{\Gamma\left(y_0\right)}{\pi V_\infty c\left(y_0\right)} + \alpha_{L=0}\left(y_0\right) + \frac{1}{4\pi V_\infty}\int_{-b}^{b}\frac{(d\Gamma/dy)dy}{y_0 - y} \tag{2.3}$$

Which states that $\alpha_{\text{eff}} = \alpha - \alpha_i$ and has Γ as the only unknown. Once Γ is found, it is possible to apply the Kutta-Jukowski theorem to get the lift and therefore the induced drag as follows:

$$L = \rho_\infty V_\infty \int_{-b}^{b}\Gamma(y)dy \tag{2.4}$$

$$C_L = \frac{L}{q_\infty S} = \frac{2}{V_\infty S}\int_{-b}^{b}\Gamma(y)dy \tag{2.5}$$

$$d_i = \ell \cdot \sin\alpha_i \tag{2.6}$$

where d and ℓ are the sectional induced drag and the sectional lift respectively. Since α_i is small, this relation becomes

$$\begin{aligned} d_i &= \ell \cdot \alpha_i \\ D_i &= \int_{-b}^{b}\ell(y)\alpha_i(y)dy \end{aligned} \tag{2.7}$$

or

$$D_i = \rho_\infty V_\infty \int_{-b}^{b}\Gamma(y)\alpha_i(y)dy \tag{2.8}$$

In turn, the induced drag coefficient is

$$C_{D,i} = \frac{D_i}{q_\infty S} = \frac{2}{V_\infty S}\int_{-b}^{b}\Gamma(y)\alpha_i(y)dy \tag{2.9}$$

2.4 Trefftz Plane Analysis

Another method to compute the induced drag can be obtained by studying the far-field effect of the wake on the surrounding fluid. The concept behind this idea is to apply momentum conservation to a control volume containing the body to be studied. In such volume, a wing can be schematized using the above-mentioned lifting-line theory and the far-field plane in which the wake is studied is typically named Trefftz plane, Figure 2.4.

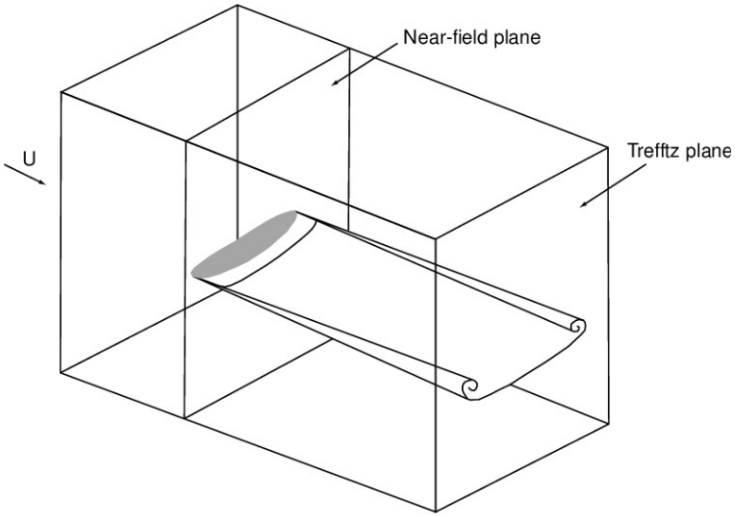

Figure 2.4: Control volume considered for Trefftz plane analysis [16].

The final equation for induced drag obtained with this method is presented in Equation 2.10. Further derivation can be easily found in literature, and therefore it is here omitted [17].

$$D_i = \frac{1}{2}\rho \iint_{S_{\text{Trefftz}}} \left(v'^2 + w'^2\right) dS \tag{2.10}$$

The terms indicated with a prime in Equation 2.10 are the velocity components perturbations in y and z direction respectively. Indeed, being the freestream velocity V_∞ parallel to the x axis the velocity components in different directions in the Trefftz plane are only due to the presence of the wake. For clarity, in Equation 2.11 the velocity components u, v, and w are symbolically expressed in terms of the freestream velocity and the perturbations due to the wake.

$$\begin{aligned} u &= V_\infty + u' \\ v &= v' \\ w &= w' \end{aligned} \tag{2.11}$$

Another definition of the induced drag comes out as a result of Equation 2.10. The induced drag is the force due to kinetic energy transfer into the crossflow, in other words the trailing edge vortices.

It is important to clearly state the assumptions on which Trefftz analysis is based on. They are listed below as presented by S.C. Smith [17]:

1. The flow is considered to be continuous, stationary, and inviscid.
2. The trailing wake is either assumed to be force-free, or to be drag-free as a result of trailing in the freestream direction. It should be noted that this assumption does not imply that the two different wake shapes would produce the same drag, but rather that the derivation is valid in both cases.

3. The flow is assumed to be isentropic and of a perfect gas, and in the vicinity of the wake, far away from the wing, it may be considered as a small perturbation from the freestream.
4. The evolution of the force-free wake is assumed to be slow enough such that u-perturbations are negligible, and as such, the flow can be considered two-dimensional in the Trefftz plane.

2.5 Vortex Lattice Method

Prandtl's lifting line theory is mainly reliable for straight wings with not too low aspect ratio. However, it is necessary to introduce a more complex model when dealing with highly swept wings like the Flying V's one. In this context the Vortex Lattice Method (VLM) can be introduced to tackle this issue and predict the aerodynamic properties of such wings.

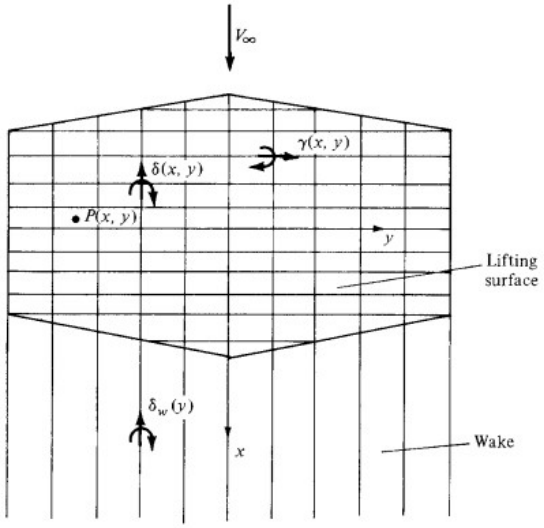

Figure 2.5: Vortex Lattice Method, wing grid-like structure scheme [13].

When the lifting line theory was introduced above, the wing was schematically represented by a series of vortices placed in a single line along the wing span. In that case, the circulation over the wing varies only in the y direction along the span itself. However, in this new adaptation of the previously presented model it is possible to introduce a series of lifting lines. It is possible to place them on the plane of the wing at different locations along the chord of each selected wing section. Such lines are crossed by the trailing vortices that develop in the freestream direction, x. In this way, the wing is represented by a grid-like scheme of vortices where each 'cell' is called a lattice and that is why this is called the Vortex Lattice Method, Figure 2.5 [13]. The vortex strength related to vortex lines does not only vary along the wingspan but also in the freestream direction, $\gamma = \gamma(x, y)$. Moreover, because in such structure the trailing vortices overlap affecting each other, also the strength of the trailing vortices varies in both x and y direction, $\delta = \delta(x, y)$. However, the strength of the vortex sheet, δ_w, developing in the wake only depends on y as no spanwise vortex lines are present in the wake. It is indeed constant in the freestream direction and equal to its value at the wing's trailing edge [13].

Once the lifting surface has been defined, the main objective is to get the unknown γ and δ while the flow tangency condition is respected over the wing by imposing that the sum of $w(x, y)$ and the normal component of the freestream velocity is zero [13].

The vortex sheet over the wing can be discretised by using a finite number of horseshoe vortices of a certain strength. For instance, the wing geometry can be panelled and each of those vortex can be placed at a distance of 1/4 of the panel's chord length from the front of the panel. A control point, where the flow tangency condition is applied, can be located on the center line at 3/4 of the panel's chord length from the front of the panel. It is then possible to compute the induced vertical velocity at any arbitrary point P by solving a system of algebraic equations coming from the application of the Biot-Savart law. A schematized representation of a paneled wing is presented in Figure 2.6.

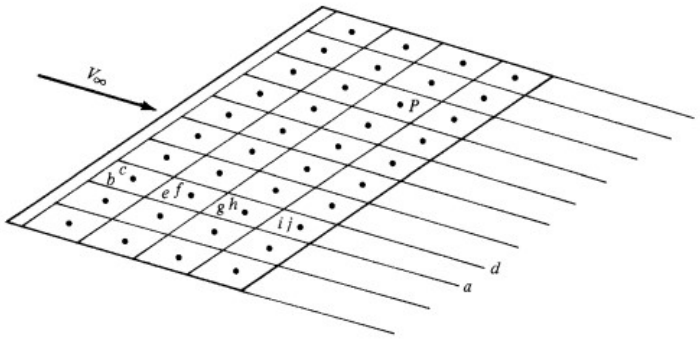

Figure 2.6: Vortex Lattice Method panelled wing [13].

2.6 Athena Vortex Lattice

Athena Vortex Lattice (AVL) is a VLM developed by M. Drela and H. Youngren at MIT in 1988 [18]. Other than predicting the aerodynamic properties of a fixed wing, AVL provides different options to the user. Indeed, the software also allows the possibility of modelling slender bodies representing fuselages and nacelles using a combination of a source and a doublet filament. In addition, AVL also supports control surfaces deflections.

2.6.1 Flow Characterization

AVL assumes an inviscid, quasi-steady flow which therefore does not take unsteady vorticity shedding into account. Compressibility is addressed by means of the classical Prandtl-Glauert correction. However, this is considered valid up to a perpendicular Mach number of about 0.7, calculated as freestream Mach number times the cosine of the eventually present wing sweep. In addition, thin airfoil theory is considered and a default airfoil lift slope of 2π is assigned unless specified by the user.

The induced drag, a property of interest for the research goal addressed in this document, can be computed both with surface force integration and with a Trefftz-plane analysis. The latter is considered more reliable [18].

2.6.2 AVL Input Data

This section discusses the input data required by AVL, with various files needed to run a simulation.

The initial file is the geometry file, which assigns reference parameters for the geometry, such as wing-span, chord, and wing area. The geometry itself is constructed by defining a surface, along with the number of chord-wise and span-wise vortices used to discretize the surface. The spacing between these vortices can be linear, cosine, or sine. Additionally, the surface is further defined by specifying sections along the wing-span, providing the leading edge coordinates and angle of incidence for each section. Furthermore, the software can read an external airfoil coordinates file using the '`AFIL`' command, utilizing the camber line of the airfoil to describe the section.
Another required file is the '`case`' file, which defines the desired flight conditions for the simulation.

An alternative approach is to use the Python [19] interface called AVLWrapper [20], as found in the available literature. This interface enables users to construct and modify the necessary files directly from the Python environment. This capability proves highly advantageous within optimization algorithms, allowing for automated initiation and analysis of simulations with varied parameters.

3

Methodology

In this chapter, a detailed overview of the methodology adopted to tackle the optimization problem at hand is provided. The chapter begins by introducing and discussing the wing parameterization. Following that, the optimization problem is presented in a formalized manner, introducing the design vector, constraints, and objective function. Subsequently, the optimization algorithm is presented and discussed, outlining the necessary steps to obtain the final results. Additionally, a simplified viscous module is introduced to enhance the estimation of the lift-to-drag ratio that needs to be computed. Furthermore, a sensitivity analysis module is presented, offering an overview of how to understand the impact of each model inputs on the output.

3.1 Parameterization

The Flying V parameterized wing geometry used for the optimization process was obtained by defining eight sections along half the wingspan, as shown in Figure 3.1. Section I is located at the wing root and Section VI is located at the wing tip. The latter, together with Section VII and Section VIII, approximates the shape of the winglet. The thicker gray line in Figure 3.1 represents the limit of the passenger's cabin shape.

Each wing Section of the inboard wing region, where the passengers cabin is located, has been modeled with a wire-frame-like configuration as shown in Figure 3.1. The presence of the cabin constrains the front part of Section I to Section IV, highlighted in red, to have a fixed inclination. This corresponds to $a_{1,\text{front}}$ in Figure 3.1 where the detail on the bottom of the figure shows a generic Section I represented with exaggerated angles for a better visualisation. The

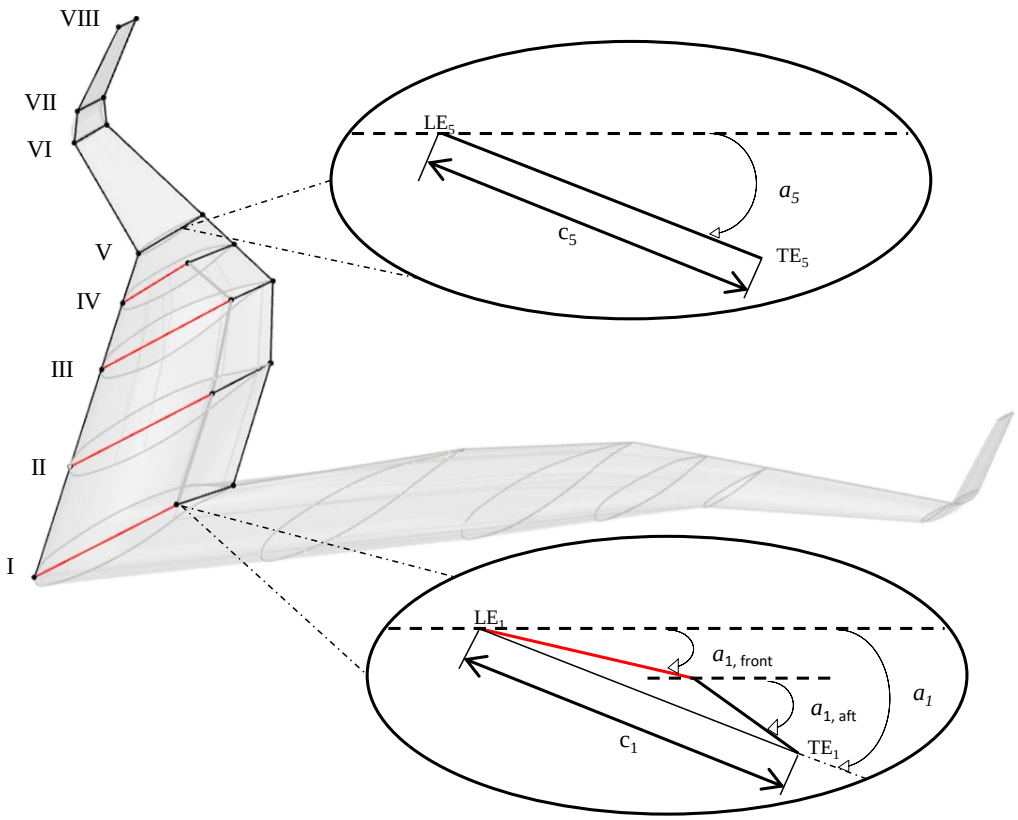

Figure 3.1: Generic parameterized wing geometry overlay with CAD geometry, with angles of interest highlighted and exaggerated for better visualization.

same schematization applies to Sections II to IV. Due to this, only the aft part of each of these sections can rotate freely during the optimization process. The angle associated to such rotation is shown in Figure 3.1 as $a_{1,\text{aft}}$. As a consequence, the camber of Sections I to IV is modified, and the position of the trailing edge is altered as well. Consequently, the resulting incidence angle, a_1 in Figure 3.1, also changes. The resulting kinked camber is then smoothed up before being fed as input to AVL, as explained in more detail later in this chapter.

On the other hand, the camber of Sections V to VIII is kept constant during the optimization process and only their incidence angle is varied. The detail shown on the upper side in Figure 3.1 offers a closer examination of Section V, emphasizing exaggerated angles. It is worth noting that this identical schematization is then consistently implemented across all the subsequent sections extending towards the wing-tip.

To ensure the effectiveness of control surfaces in the outboard wing region, the trailing edge between Sections III to VI must remain straight. Therefore, it is the dihedral Γ of the outboard wing, highlighted in Figure 3.2, that determines the position of the trailing edge of these Sections,

which can vary during optimization. As a result, the dihedral angle directly influences the incidence angle of the aft portion of Section IV, which is not a direct design variable like the aft portion of the other inboard wing Sections. However, the incidence angles of the remaining outboard wing Sections are adjustable during the optimization, with rotation occurring around their trailing edge to maintain a straight trailing edge as previously stated.

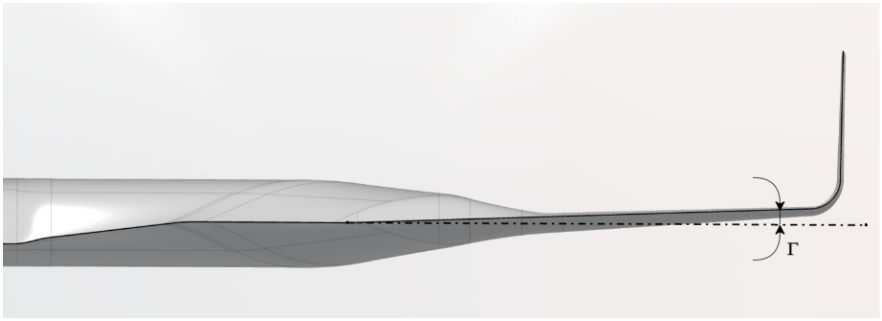

Figure 3.2: Back view of the Flying V wing with outer wing dihedral highlighted, snapshot taken from the CAD model.

3.2 Optimization

A comprehensive description of the optimization process is provided in this section. Initially, the problem is formalized using mathematical notations, as specified in Section 3.2.1. Following that, a detailed overview of the optimization algorithm is presented in Section 3.2.2.

3.2.1 Problem Formalization

This section focuses on the optimization process implemented to get to the minimum induced drag design. It can be expressed in mathematical notation as follows:

$$\begin{aligned} \min_{\bar{y} \in R^n} \quad & C_{D_i}(\bar{y}) \\ \text{s.t.} \quad & \bar{g}(\bar{y}) \leq 0 \end{aligned} \tag{3.1}$$

In particular, the induced drag coefficient that needs to be minimized is computed using AVL with a Trefftz-plane analysis, which is considered more accurate than the induced drag coefficient obtained from surface-force integration [18]. The design vector $\bar{y}$ consists of various parameters such as the incidence angle of the aft part of Sections I to III, the dihedral angle Γ that determines the position of the trailing edge point of Sections IV to VI, and the incidence angle of Sections V to VIII. This leads to a total of 8 design variables. The only bounded variable is Γ, although the optimized value of this variable never reaches the imposed bounds of 1° and 3°. The design vector is shown below:

$$\bar{y} = (a_{1,\text{aft}}, a_{2,\text{aft}}, a_{3,\text{aft}}, \Gamma, a_5, a_6, a_7, a_8) \tag{3.2}$$

The inequality constraints $\bar{g}(\bar{y})$ are necessary to ensure the feasibility of the optimization results.

The first constraint is related to the resulting angle of attack computed by AVL once the geometry has been defined and the lift coefficient provided as input. Different values of the angle of attack constraint have been investigated because it significantly affects the final results, as discussed in Chapter 5. The second constraint ensures a positive distance between the neutral point of the aircraft and the center of pressure. Specifically, it is required to be at least 2% of the Mean Aerodynamic Chord ($\bar{c}$), serving as a measure of the aircraft's static margin. A standard transport aircraft typically maintains a static margin of up to 5% of the Mean Aerodynamic Chord [21, 22]. However, due to the Flying V's mean aerodynamic chord being twice as large as the aircraft in the same category of the Flying V, a static margin of 2% of the mean aerodynamic chord is opted for, ensuring a comparable absolute distance. The constraints can be expressed mathematically as follows:

$$\begin{aligned} \alpha &\leq \alpha_{\text{value}} \\ X_{\text{NP}} - X_{\text{CP}} &\geq 0.02 \cdot \bar{c} \end{aligned} \tag{3.3}$$

AVL performs computations to determine the angle of attack, neutral point location (X_{NP}), and the other relevant aerodynamic coefficients based on the provided lift coefficient and wing geometry. The center of pressure location X_{CP} is calculated by treating the total lift as a single vector and locating the point where the moment generated by this vector equals the total pitching moment calculated by AVL. The estimation of X_{CP} can be described by the equation below, where C_m represents the total pitching moment coefficient, C_L represents the lift coefficient, and $\bar{c}$ represents the mean aerodynamic chord:

$$X_{\text{CP}} = \frac{C_m}{C_L} \cdot \bar{c} \tag{3.4}$$

.

3.2.2 Optimization Algorithm

In this subsection, the optimization algorithm implemented to address the current optimization problem is discussed. An overview of this algorithm is presented in Figure 3.3.

To begin, the initial design configuration is considered, and the parameters for wing geometry and airfoil shapes are exported from the CAD model. Subsequently, the parameterized wing geometry is constructed, and the design vector is defined. The initial values for the design variables are set based on the previous step. Next, the design vector is passed to the optimizer, which executes an AVL simulation using the current design vector values. The optimizer obtains the results and verifies both convergence and constraints. If the requirements are not met, the process returns to the design vector, and the iteration begins again.

In addition to this conventional optimization approach, a manual feedback loop is incorporated

between the completion of the pure optimization process and the final stage of the procedure. This feedback loop is necessary to align the purely optimized geometry with the CAD model geometry. Since the two parameterizations are fundamentally distinct, with the latter being considerably more intricate than the former, achieving a perfect match between the two is not feasible. Consequently, once the CAD geometry has been adjusted to match the purely optimized one within the feedback loop, another AVL simulation is performed. This simulation aims to identify any disparities between the results obtained from the optimization process and the adjusted CAD geometry. The process continues until a satisfactory correspondence is achieved between the two. Once a satisfactory alignment is obtained, the entire process is considered complete.

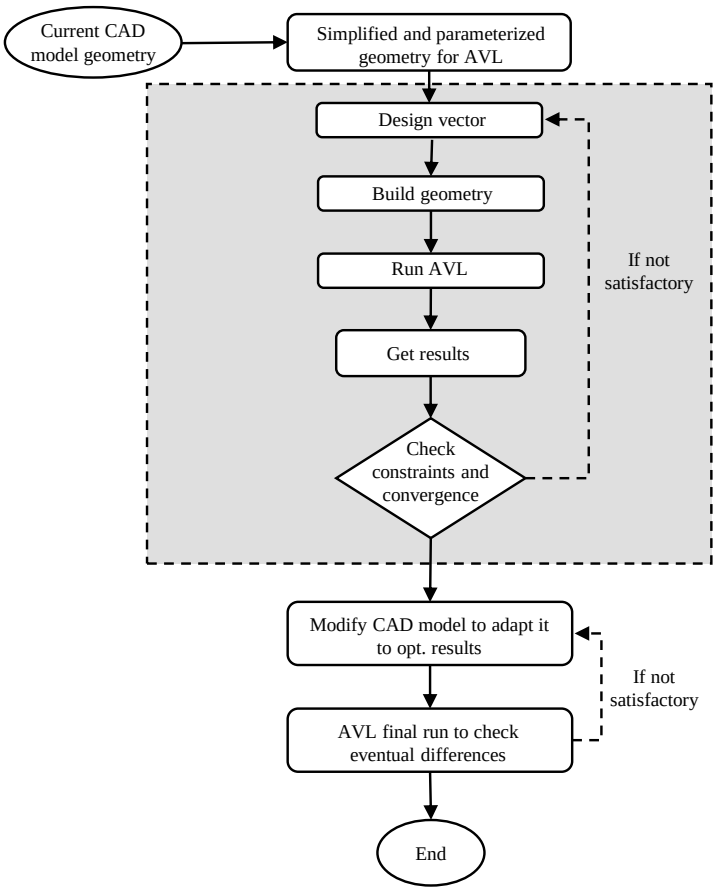

Figure 3.3: Optimization process flowchart.

It is important to delve into the sub-algorithm that is responsible for defining the parameterized geometry and preparing it for the subsequent AVL simulation. A visual representation of this process is depicted in Figure 3.4.

After the optimizer updates the design vector, the wireframe configuration mentioned earlier can be constructed. However, AVL requires reading airfoil coordinates from external files in order to accurately replicate the camber line shape of each airfoil. Thus, the construction of camber for Sections I to IV is performed by an external routine, which follows the steps outlined below.

Firstly, it takes the front part's camber line from the initial design configuration, ensuring that the shape and inclination remain unaltered to comply with the geometrical constraints associated with the presence of the passengers' cabin. Subsequently, a straight line is appended to this front part, with a rotation angle determined by the optimizer, representing a simplified version of the aft part of the section. To avoid a sharp kink in the camber line, which deviates significantly from a realistic airfoil camber line, a polynomial interpolation is employed to smoothen it. This interpolation eliminates the kink and results in a smoother camber line.

Once the camber line has been adjusted, the airfoil coordinates are written to external files that AVL can read by maintaining the same thickness distribution as the initial design airfoils. With these files prepared, the geometry can be constructed by utilizing the wing planform data, the design variables updated by the optimizer, and the newly created external airfoil files. Consequently, the geometry is now ready to be used for an AVL simulation.

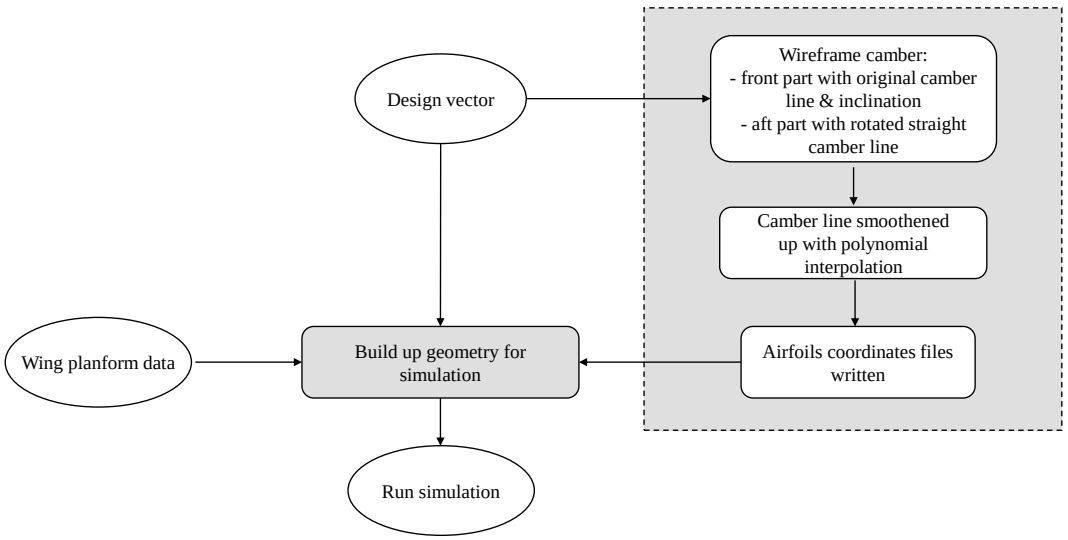

Figure 3.4: Geometry definition process flowchart.

The algorithm used by the optimizer is the Constrained Optimization by Linear Approxima-

tion (COBYLA) algorithm introduced by Michael J. D. Powell [23]. This method is usually employed for constrained problems with unknown or computationally expensive derivatives of the objective function and constraints. It is a gradient-free and trust-region method, which means that it adapts the size of the trust region to the current state of the optimization making convergence faster. The initial step of the changes to the variables can be varied to verify the robustness of the optimized design variables and objective function. The most common optimization algorithm used in Python [19] to find the minimum of an objective function is probably *scipy.optimize.minimize* [24]. This function is part of the *SciPy* library [25] and it provides a unified interface to various optimization methods, including COBYLA algorithm. This function is a wrapper around many optimization algorithms and it is very versatile and easy to use, which is why it is commonly used in Python.

3.3 Viscous Module

The vortex lattice method is only able to compute the induced drag. Thus, a simplified viscous module can be introduced in order to get a better estimate of the overall lift-to-drag ratio. In particular, the profile drag can be estimated through an empirical method [21, 26]. The profile drag is comprised of three components, namely skin friction, pressure, and lift-related profile drag. However, for the purpose of analyzing the flight conditions considered in this study the third component can be ignored [27]. Therefore, the remaining two components are simultaneously addressed using the following formulation:

$$C_{D_v} = C_F \cdot f \cdot \frac{S_{\text{wet}}}{S} \tag{3.5}$$

That can be applied to each of the Flying V components which are the wing and the winglets in this case. C_F is the flat plate skin friction coefficient, f is the form factor of each of the components considered, S_{wet} is the wetted area, estimated through the CAD model available, and S is the reference area. The wing form factor and the flat plate skin friction coefficient can be computed with semi-empirical equations [26, 28] as shown:

$$f = 1 + \left(2.7 \cdot \frac{t}{c} + 100 \cdot \left(\frac{t}{c} \right)^4 \right) \cos^2 \left(\Lambda_{0.5} \right) \tag{3.6}$$

$$C_F = \frac{0.455}{\left(\log_{10} Re \right)^{2.58} \left(1 + 0.144 \cdot M^2 \right)^{0.65}} \tag{3.7}$$

where $\frac{t}{c}$ is the thickness to chord ratio of each strip and $\Lambda_{0.5}$ is the mid chord sweep angle. Consequently, the overall aerodynamic efficiency C_L/C_D can be computed as:

$$\frac{C_L}{C_D} = \frac{C_L}{C_{D_i} + C_{D_v}} \tag{3.8}$$

3.4 Sensitivity Analysis

A sensitivity analysis was performed to assess the influence of each model input on the model output and their interactions. This approach offers a detailed and comprehensive understanding of the model's behavior, aiding in decision-making, model improvement, and uncertainty reduction in complex systems. In particular, the Morris method, or Elementary Effects (EE) method, was employed and a brief overview is presented in this section. More details can be found in [29]. The analysis was performed in this study by implementing the method with the Python SALib library [30].

The Morris method for sensitivity analysis involves exploring the design space using trajectories. Each trajectory represents a set of parameter combinations, with each parameter being varied individually while others are held constant. These trajectories are generated by assigning a reference value to each parameter and randomly perturbing it within defined intervals.

To quantify the influence of parameters on the model output, the Morris method calculates elementary effects. An elementary effect measures the difference in the model output caused by varying a single parameter while keeping the others fixed at different levels. Trajectories are constructed by randomly selecting parameter values along each dimension and recording the corresponding model outputs. By generating multiple trajectories and evaluating the corresponding elementary effects, the Morris method provides insights into parameter importance and interactions. It helps identify influential parameters that significantly affect the model output and those that have minimal impact. Trajectories are designed to thoroughly explore the parameter space, covering various ranges and combinations of parameter values. This ensures a comprehensive assessment of parameter influence and sensitivity.

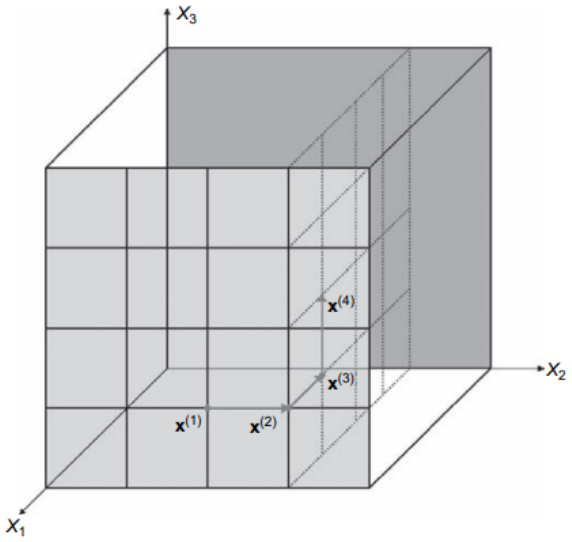

Figure 3.5: An example of a trajectory in the input space, Saltelli et al. [29].

The Morris method employs statistical measures, such as μ, μ^*, and σ, to summarize and interpret the sensitivity analysis results. The mean μ represents the average effect of a parameter across all trajectories, providing an estimation of its impact on the model output. The absolute mean μ^* calculates the average absolute effect of a parameter, indicating its overall magnitude irrespective of direction. The standard deviation σ quantifies the within-trajectory variation of the elementary effects, reflecting the degree of parameter interactions and potential nonlinear relationships.

These statistical measures aid in prioritizing parameters for further investigation or refinement. By considering these values together, it is possible to gain a deeper understanding of parameter behavior and to make informed decisions to enhance the model's reliability and understanding.

If μ is close to zero, it suggests that the parameter has a minimal overall effect on the model output. Changes in this parameter are unlikely to significantly influence the output. On the other hand, if μ is significantly positive or negative, it indicates that the parameter has a substantial average effect on the model output. Positive values suggest that increasing the parameter value tends to increase the output, while negative values imply the opposite.

If μ^* is close to zero, it implies that the parameter has relatively small absolute effects on the model output. The magnitude of its impact, regardless of the direction, is not significant. On the other hand, if μ^* is relatively high, it suggests that the parameter has large absolute effects on the model output. This means that variations in the parameter have a substantial impact, regardless of whether they increase or decrease the output.

If σ is small, it indicates low within-trajectory variation of the elementary effects for the parameter. This suggests that changes in the parameter have consistent and predictable effects across different trajectories. However, if σ is large, it suggests significant within-trajectory variation of the elementary effects. This implies that the impact of the parameter on the model output is influenced by interactions with other parameters, indicating potential nonlinearity or complex dependencies.

Parameters with high values of μ and μ^* indicate influential factors that consistently and significantly impact the output. On the other hand, parameters with high μ^* but low μ values suggest that their impact is more uncertain or context-dependent, as the direction of their effect varies across different trajectories. Additionally, parameters with large σ values indicate complex interactions and dependencies with other parameters, highlighting the need for further investigation into their combined effects.
The mentioned statistics are defined in a mathematical form below where EE_i^j indicates the elementary effects relative to the design variable i computed along trajectory j [29]:

$$EE_i^j = \frac{f\left(x_i^j + \Delta x_i^j\right)}{\Delta x_i^j} \tag{3.9}$$

$$\mu_i = \frac{1}{r}\sum_{j=1}^{r} EE_i^j \tag{3.10}$$

$$\mu_i^* = \frac{1}{r}\sum_{j=1}^{r} \left|EE_i^j\right| \tag{3.11}$$

$$\sigma_i^2 = \frac{1}{r-1}\sum_{j=1}^{r} \left(EE_i^j - \mu\right)^2 \tag{3.12}$$

with $i = 1, \ldots, k$ and $x^i \in \boldsymbol{X}^j$ as well as $j = 1, \ldots, r$ and $\boldsymbol{X}^j \in \boldsymbol{\Pi}$.

4

Validation

This chapter is dedicated to the validation study conducted to assess the performance of AVL in predicting aerodynamic quantities of interest. The Onera M6 wing was selected as a case study, with available experimental data on pressure coefficients at various locations along the wingspan for different Mach numbers, as presented by V. Schmitt and F. Charpin [31]. The pressure coefficient distribution at each section can be integrated to derive the local lift coefficient, denoted as C_ℓ, which was subsequently compared to the corresponding value calculated by AVL using the identical geometry. In addition, a brief verification of the neutral point calculation obtained using AVL is presented.

4.1 Case Study - Onera M6

The Onera M6 wing is a simple swept-back wing that has been widely used for validation purposes throughout the years. Experimental data for this wing are available as it was tested at transonic Mach numbers ranging from 0.7 up to 0.92 and at several angles of attack from 0° to 6°. The mean aerodynamic chord-based Reynolds number used during the experiments is about $12 \cdot 10^6$ [31].

The Onera M6 wing is considered a standard validation case, particularly for CFD validation of external flows, owing to its combination of simple geometry and the complexities arising from transonic flow [32]. Figure 4.1 illustrates the wing geometry and key geometrical parameters. The sections where pressure taps were positioned commence at 20% of the wingspan to avoid erroneous data caused by the interaction between the wall and the flow over sections nearer to the root. The spacing between these sections is progressively reduced towards the wingtip to

enhance data accuracy in this critical flow region.

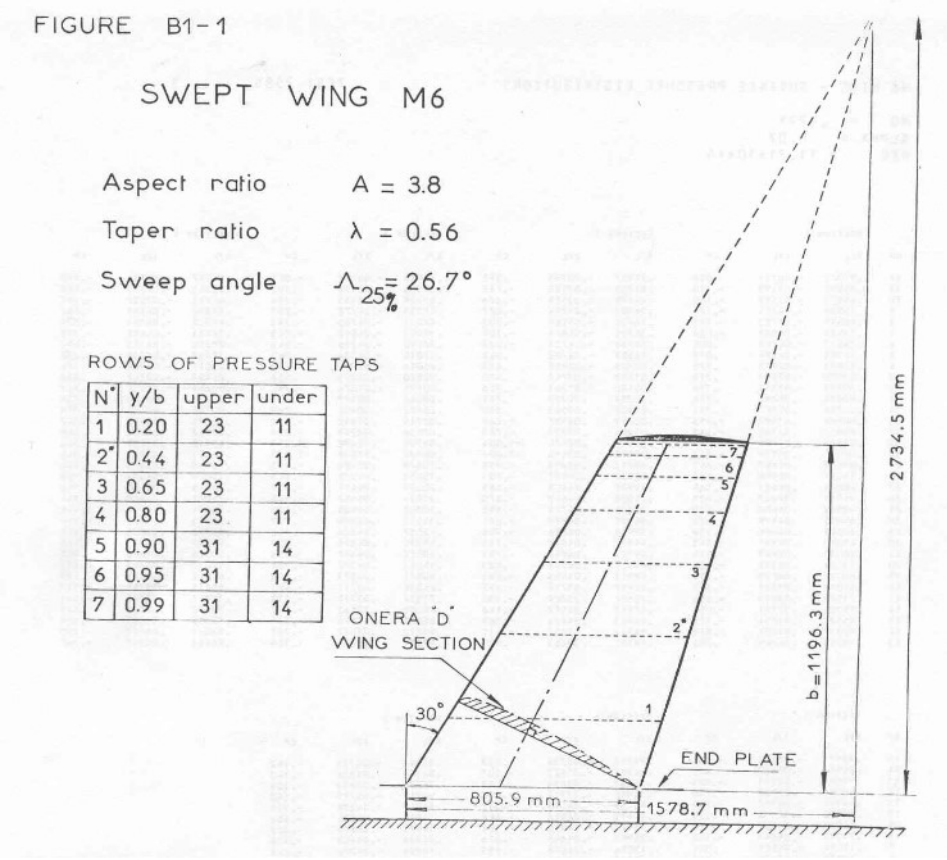

Figure 4.1: Onera M6 wing geometry Fig. B1-1 in [31]

As mentioned in the previous section, AVL makes use of the Prandtl-Glauert correction to take into account compressibility effects. It is important to underline that such correction assumes small perturbations, thus thin surfaces, and it can become invalid when the perturbations to the free stream are too large. In general, the importance of compressibility effects, and therefore the validity of such correction, can be assessed by considering the Prandtl-Glauert factor shown in Equation 4.1 [18]. The range of validity in terms of Mach number is shown in Figure 4.2.

$$PG = \frac{1}{\sqrt{1 - M^2}} \tag{4.1}$$

However, it is important to notice that when dealing with a swept wing the Mach number to be considered is the wing-perpendicular one. This can be easily obtained by multiplying the free stream Mach number for the cosine of the wing sweep angle, which for the Onera M6 wing is equal to 30°.

For this reason, among the ones available in the experimental data, the Mach number chosen to be reproduced computationally by using AVL is 0.7. It is possible to verify that the Prandtl-

M	$\frac{1}{B}$	
0.0	1.000	PG expected valid
0.1	1.005	
0.2	1.021	
0.3	1.048	
0.4	1.091	
0.5	1.155	
0.6	1.250	
0.7	1.400	PG suspect (transonic flow likely)
0.8	1.667	PG unreliable (transonic flow certain)
0.9	2.294	PG hopeless

Figure 4.2: Mach number range of validity for Prandtl-Glauert correction applied in AVL [18], where PG stands for Prandtl-Glauert correction factor.

Glauert factor for this flow condition and the Onera M6 wing is 0.61, which falls within the validity range shown in Figure 4.2.

The flow conditions simulated with AVL and compared with the experimental data are listed in Table 4.1.

Table 4.1: Flow conditions simulated in AVL to analyse Onera M6 wing.

M [−]	Re [−]	α [°]
0.7	$11.72 \cdot 10^6$	2
0.7	$11.72 \cdot 10^6$	4
0.7	$11.72 \cdot 10^6$	6

4.1.1 Onera M6 - Experimental Data

The experimental data is available in form of pressure coefficient distribution over the sections along the wingspan. Therefore, such data had to be processed to get the lift distribution over the wing. The sectional lift coefficient is obtained by computationally calculating the area enclosed by the pressure coefficient distribution curve, which is the graphical meaning of Equation 4.2 which relates the two quantities analytically.

$$C_\ell = \frac{1}{x_{TE} - x_{LE}} \int_{x_{LE}}^{x_{TE}} \left(C_{p_l}(x) - C_{p_u}(x)\right) dx \tag{4.2}$$

In a similar way, the total lift coefficient can be found integrating the sectional lift coefficients along the wingspan as shown in Equation 4.3 for half of the wing.

$$C_L = \int_{-b}^{b} C_\ell(y)\ c(y)\ dy \tag{4.3}$$

As a reference, the experimental pressure coefficient distributions along the wingspan of the Onera M6 wing are shown in Figure 4.3 for 3° angle of attack.

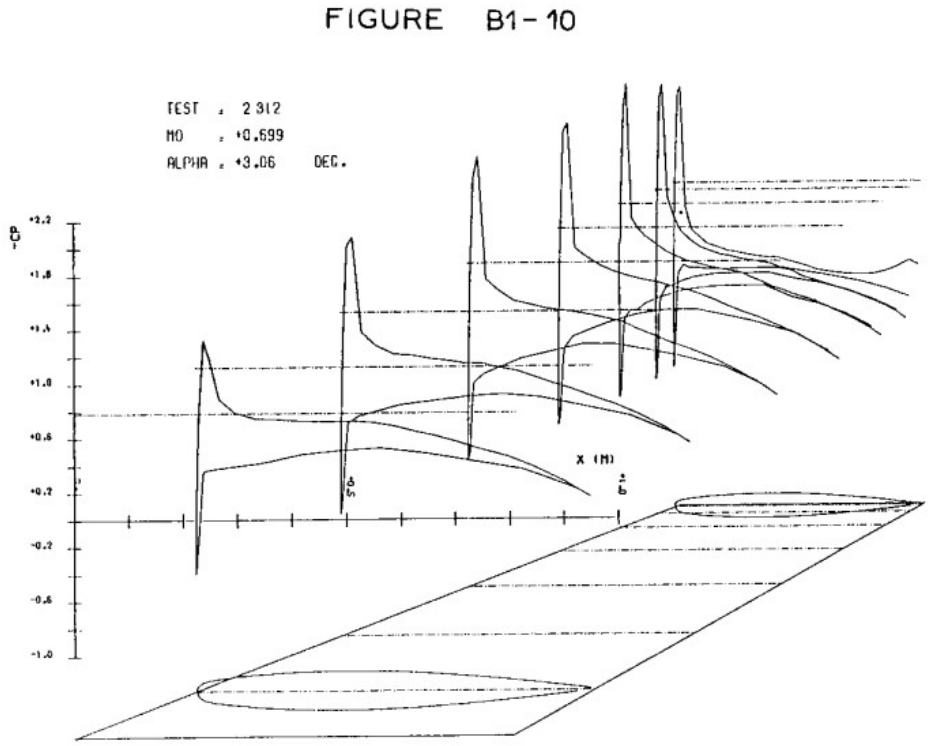

Figure 4.3: Experimental pressure coefficient distributions along the wingspan of the Onera M6 wing Fig. B1-10 [31].

4.1.2 Onera M6 - AVL Data

The wing geometry was obtained by defining the root section and the tip one, using the original symmetric airfoil present on the Onera M6 wing. The wing geometry is shown in the AVL environment in Figure 4.4.

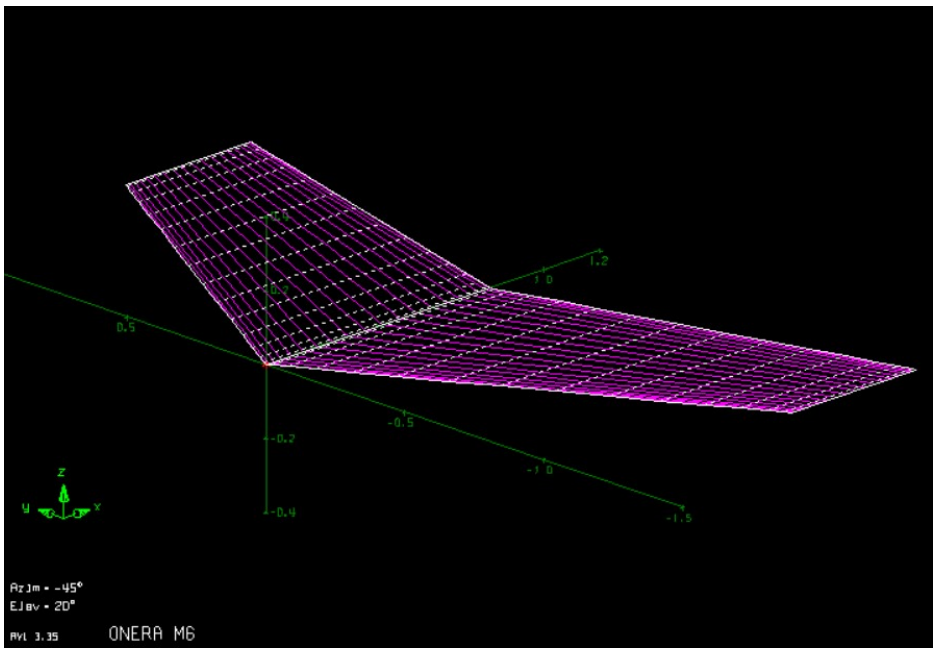

Figure 4.4: Onera M6 wing geometry in AVL

The flow conditions of the experiments were reproduced in AVL by defining the angle of attack, Mach number, and Reynolds number in the software's case file.

4.1.3 Comparison Between Experimental Data and AVL Calculated Data

The data calculated with AVL is compared to the experimental data in this section. In particular, that is shown in Figure 4.5 where the lift distribution is presented for each angle of attack considered. The experimental data do not exactly cover the whole wingspan because the pressure taps were located between the 20% of the wingspan and the wing tip.

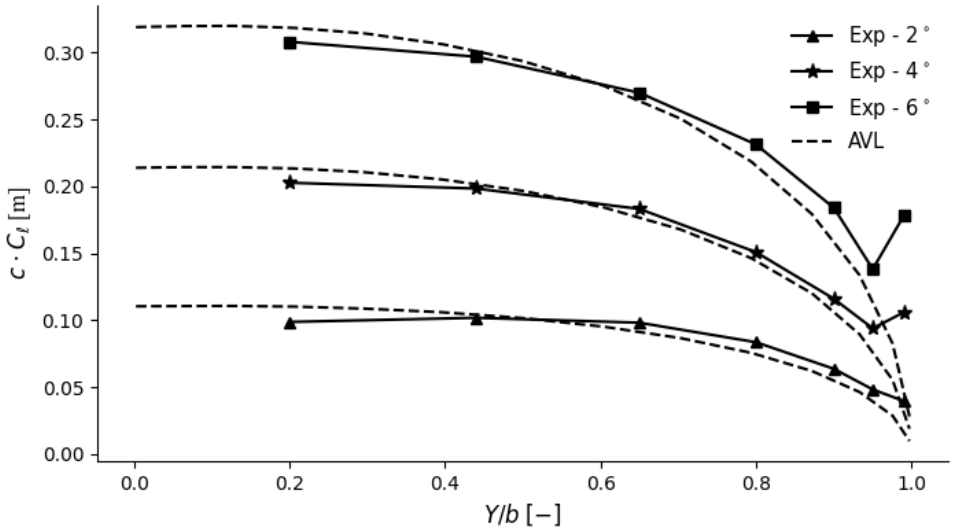

Figure 4.5: Onera M6 experimental data vs AVL data for lift distribution.

It is possible to notice that the lower the angle, the higher the discrepancies between the two data sets close to the root region. However, it has to be considered that in the experimental set up the root region is the closest to the wall to which the wing is attached, and therefore the flow is affected by it. This could lead to the mentioned differences with the calculations made using AVL. It would be necessary to use a more accurate solver, like CFD, to investigate deeper the matter. Considering the overall results and the scope of this part of the research, AVL performance was deemed accurate enough. The difference between the total lift coefficient measured during the experiments and the one calculated with AVL is shown in Table 4.2 for each angle of attack studied. The results are deemed satisfactory as it is also necessary to consider that the software was operating at the limit of the range of validity of the Prandtl-Glauert correction.

The discrepancies present at the wing tip between the two data sets are to be found in a highly likely experimental mismeasurement. This can also be noticed in Figure 4.3, where the pressure coefficient distribution at the wing tip shows an unusual shape towards the trailing edge of the

Table 4.2: Comparison between the experimental lift coefficient and calculated one

	$\alpha = 2°$	$\alpha = 4°$	$\alpha = 6°$
$C_{L_{\text{exp}}}$	0.140	0.284	0.437
$C_{L_{\text{AVL}}}$	0.146	0.284	0.424
Error	+4.1%	-0.001%	-3.0%

relative section.

4.2 Neutral Point Verification

This section provides a concise verification of AVL's automated neutral point location calculation. To ensure its accuracy, the verification process involves placing the reference point at the neutral point calculated by the software and examining the pitching moment coefficient derivative with respect to the angle of attack. As per its definition, this derivative should equal zero when a null static margin is considered, as the moment coefficient remains unaffected by the angle of attack under such circumstances. The investigation was carried out for the Flying V's wing in a range of angles of attack interesting for the study at hand. The results displayed in Figure 4.6, demonstrate the expected neutral static stability and therefore the accuracy of the AVL's neutral point location calculation. A similar approach can be found in [9], used to verify the neutral point location calculation through another VLM's software.

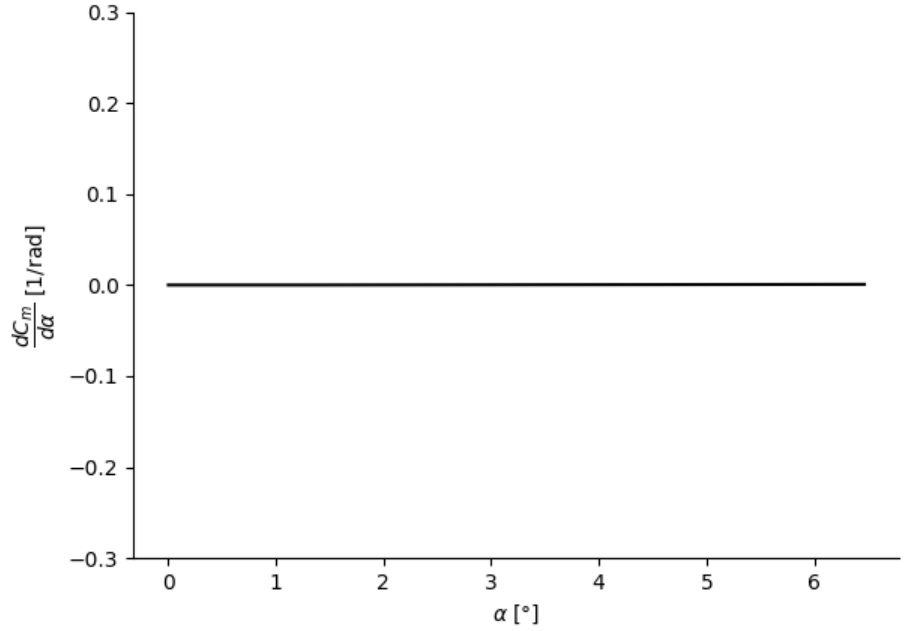

Figure 4.6: Moment coefficient derivative with respect to the angle of attack at 0% static margin.

4.3 Compressibility Correction Verification

As previously mentioned, AVL employs the Prandtl-Glauert correction to account for compressibility effects. Consequently, it becomes essential to investigate the influence of this correction on the case of the Flying V's wing. If the compressibility correction significantly affects major aerodynamic characteristics, the estimation made by AVL could lead to inaccurate results. Specifically, understanding the correction's impact on the resulting angle of attack, utilized in the calculations, is of paramount importance. An inaccurate estimation of this quantity could lead to an unfeasible design due to the constraint pertaining to the inclination of the passengers' cabin.

This can be indirectly analyzed by examining the effect of the compressibility correction on the lift-curve slope. The approach proposed by [33] for a swept wing is presented below, where the lift coefficient derivative with respect to the angle of attack modified by the Prandtl-Glauert correction, $(C_{L_\alpha})_M$, is compared to the one at 0 Mach number, $(C_{L_\alpha})_{M=0}$.

$$\frac{(C_{L_\alpha})_M}{(C_{L_\alpha})_{M=0}} = \frac{\text{Æ}R + 2\cos\Lambda}{\text{Æ}R \cdot \beta + 2\cos\Lambda} \tag{4.4}$$

In the equation above, β represents another way of representing the PG factor introduced in Equation 4.1 while also taking into account the wing sweep angle, as shown below:

$$\beta = \sqrt{1 - M^2 \cos^2\Lambda} \tag{4.5}$$

The cranked Flying V's wing presents different sweep angles between the inboard wing region and the outboard one. For this reason, it is necessary to estimate an equivalent sweep angle, Λ_{eq}, which can then be used in Equation 4.4. Many ways to compute a wing's equivalent planform shape exist in literature but for the scope of this part of the research, a rather simple method introduced by S. Gudmundsson [14] was adopted. In particular, the equivalent sweep angle is obtained by computing a weighted average of the sweep angle of each panel of the cranked wing considered with respect to their surface area. A representation of the Flying V's wing divided into such panels is shown in Figure 4.7, while the analytical expression summarising such a method is:

$$\Lambda_{eq} = \frac{2}{S} \sum_{i=1}^{5} \Lambda_i \cdot S_i \tag{4.6}$$

where Λ_i is the sweep angle and S_i is the surface area of the i_{th} panel, with $i = 1, ..., 5$. The equivalent sweep angle value obtained is presented below together with the consequent result of Equation 4.4 for $M = 0.6$:

$$\Lambda_{eq} = 61.14° \tag{4.7}$$

$$\frac{(C_{L_\alpha})_M}{(C_{L_\alpha})_{M=0}} = 1.038 \tag{4.8}$$

Therefore, the corrected lift-curve slope is 3.8% higher than the non-corrected one. This implies that in order to get the same total lift coefficient, a 3.8% lower angle of attack would be needed in the corrected case. Due to the magnitude of the target angle of attack considered in this study, specifically set at 3.5° as explained later in more detail, the difference between the corrected case and the non-corrected one would only be of the order of 0.1°. This is negligible and therefore the compressibility correction does not risk compromising the validity of the angles of attack considered in this study.

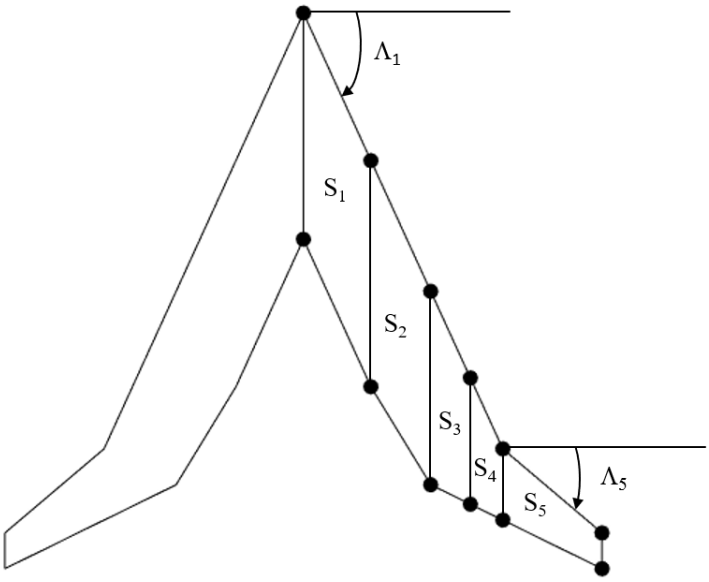

Figure 4.7: Flying V's wing planform divided into panels for equivalent wing sweep calculation

In addition, with the Λ_{eq} value obtained the resulting PG factor is equal to 1.045, which nicely falls inside the Prandtl-Glauert correction validity range shown in Figure 4.2.

5

Results & Discussion

This chapter presents and discusses the findings of the research. First the sensitivity analysis results are discussed, which highlight the influence of each model input on the corresponding output. Subsequently, the results obtained for the profile drag calculation are presented, followed by a comprehensive discussion on the optimization results. The focus is placed on the objective function, constraints values, and the resulting lift distributions. Furthermore, the chapter explains the methodology employed to obtain the final design and provides an analysis of the relative results. Specifically, the discussion encompasses the induced drag coefficient, lift-to-drag ratio, lift and induced drag distributions along the wing-span, modifications made to the inboard-wing airfoils, and a comparison of the drag polar and lift-to-drag ratio curve with those of the initial design.

The aerodynamic design optimization took place at a Mach number of 0.6 and a lift coefficient of 0.26, representing a subsonic cruise condition. However, in actuality, the Flying V would operate at a higher Mach number of 0.85 while maintaining the same lift coefficient used in this study. To achieve this consistent lift coefficient at the lower Mach number studied, a higher angle of attack than the one expected for real cruise conditions is considered. This approach ensures that when transitioning from subsonic to real cruise conditions, the aircraft can fly at a faster speed while generating the same lift coefficient at a lower angle of attack. Consequently, the angle of attack can be decreased to a level that guarantees a feasible inclination of the passengers' cabin during the real cruise phase.

Some wing planform parameters, which remained constant and unchanged throughout the optimization process, are provided in Table 5.1 and represented in Figure 5.1

Table 5.1: Description of wing planform parameters

Planform Parameter	Symbol [unit]	Value
Surface area	S [m^2]	892.00
Wing-span	$2b$ [m]	65.05
Root chord	c_r [m]	22.56
Taper ratio	λ [−]	0.16
Leading edge sweep angle 1	Λ_1 [°]	64.30
Leading edge sweep angle 2	Λ_2 [°]	38.86

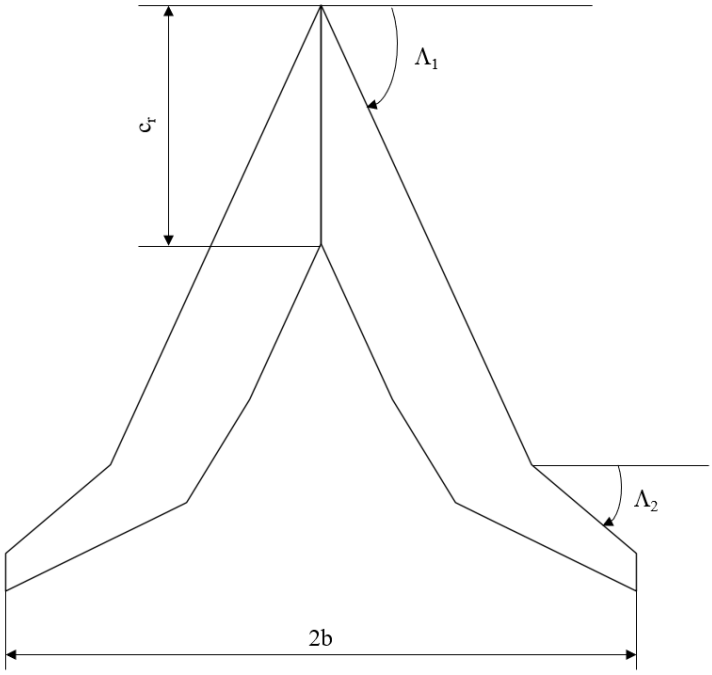

Figure 5.1: Wing planform parameters.

5.1 Sensitivity Analysis

The results of the sensitivity analysis performed are presented in this section. The analysis employed a total of 100 samples and 4 levels. This setup resulted in 900 evaluations of the objective function, encompassing a range of perturbations across the variables. The selected number of samples and levels aimed to strike a reasonable trade-off between resolution and computational feasibility. In this initial attempt, the variables were bounded between $-5°$ and $5°$, except for the variable Γ, which had bounds between $1°$ and $3°$ just like in the optimization process. The resulting statistics for each variable are shown in Figure 5.2.
The calculated sensitivity indices, including the mean, normalized mean, standard deviation, and confidence interval for the normalized mean, reveal the relative importance and variability of each variable.

Upon examining the results, it can be observed that the variables exhibit different levels of impact on the objective function. For instance, variables a_5 and $a_{3,\mathrm{aft}}$ demonstrate the largest normalized mean values. This suggests that variations in these variables have a relatively stronger influence on the objective function compared to the other variables. On the other

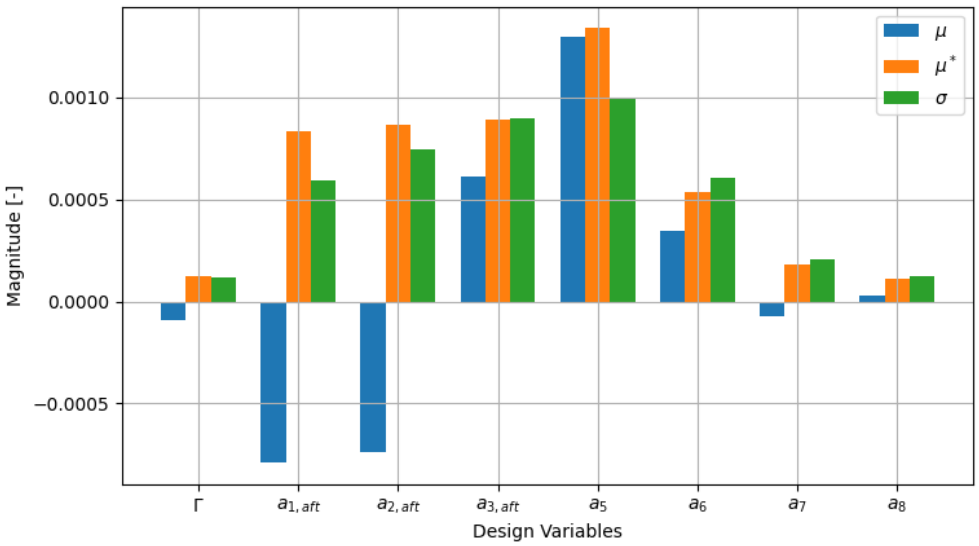

Figure 5.2: Sensitivity analysis results.

hand, variables Γ, a_7, and 8 exhibit smaller normalized mean values, indicating a relatively lower impact on the objective function.

Moreover, the standard deviations provide insights into the variability or uncertainty associated with each variable's influence. Larger standard deviation values, such as for a_5 and $a_{3,\text{aft}}$, suggest that these variables exhibit more variability in their effects on the objective function. Variables with smaller standard deviations, such as Γ and a_7, demonstrate relatively more consistent impacts.

In addition, the resulting confidence intervals for the normalized mean, which provide a measure of the estimation uncertainty, are relatively small for all variables. This indicates a reasonable level of confidence in the estimated normalized mean values, enhancing the reliability of the sensitivity analysis results.

Overall, these findings highlight the varying degrees of importance and variability among the variables in relation to the objective function. Such insights can guide decision-making processes and help prioritize resources for further investigation or optimization efforts.

5.2 Viscous Drag

The estimation of the viscous drag component was performed solely for the baseline design, and this same estimation was utilized to calculate the overall aerodynamic efficiency for all optimization cases. The obtained value, displayed below, accounts for approximately 50% to 60% of the total computed drag coefficients. This result aligns well with existing literature

[34] given the simplification implemented in this study, which includes neglecting certain drag components like wave drag and interference drag.

$$C_{D_v} = 0.00687 \tag{5.1}$$

5.3 Optimization Results

The values corresponding to the constraints and objective function for each optimization scenario are presented in Table 5.2. The optimization cases are identified using α_{value} to differentiate them, while the term baseline refers to the initial design. Among the various α_{value} used for conducting the optimizations, only the results of three cases are described in this section in order to prevent the plots from becoming too crowded. In particular, one with a freely to change α_{value}, representing no constraint, another positioned approximately in the middle of the range of values used, namely 4.5°, and the third being the lowest value employed, specifically 3.8°.

The distance between the neutral point and the center of pressure is significantly reduced for each optimized configuration compared to the baseline, nearly reaching the constraint limit. The induced drag coefficient consistently decreases in each case. Specifically, as the constraint-imposed α_{value} increases, the C_{D_i} decreases. Consequently, this outcome also influences the resulting aerodynamic efficiency. The trend of these values at different imposed angles of attack can be visualized in Figure 5.3.

Table 5.2: Comparison of resulting constraints and objective function for optimizations at different α constraint values

Case	$X_{\text{NP}} - X_{\text{CP}}$ $[m]$	α [°]	C_{D_i} $[-]$	C_L/C_D $[-]$
Baseline	2.430	6.34	0.00458	22.7
$\alpha_{\text{value}} = 3.80°$	0.434	3.70	0.00405	23.8
$\alpha_{\text{value}} = 4.50°$	0.495	4.47	0.00387	24.2
$\alpha_{\text{value}} =$ free	0.481	5.47	0.00384	24.3

The optimized values of the design variables for each optimization run are presented in Table 5.3. The resulting twist distribution, including the winglet, is illustrated in Figure 5.4. The Y axis represents the spanwise position, ranging from the wing root to the winglet tip, where it turns 90° upward towards the conventionally defined Z axis at the wing tip. Specifically, $Y = 0$ corresponds to the wing root, $Y = 1$ corresponds to the wing tip, and $Y > 1$ represents the winglet region. This chosen definition enhances the visualization of the results for both the wing and winglet, while optimizing the scaling in the provided graphs. Additionally, vertical gray dashed lines are depicted in each graph, indicating the positions of the sections along the wing span used to construct the geometry as explained in Chapter 3. Notably, the resulting twist distribution follows a similar trend for each case, exhibiting almost identical values for Sections II to IV across all cases. The primary distinction lies in the twist angle of the root section,

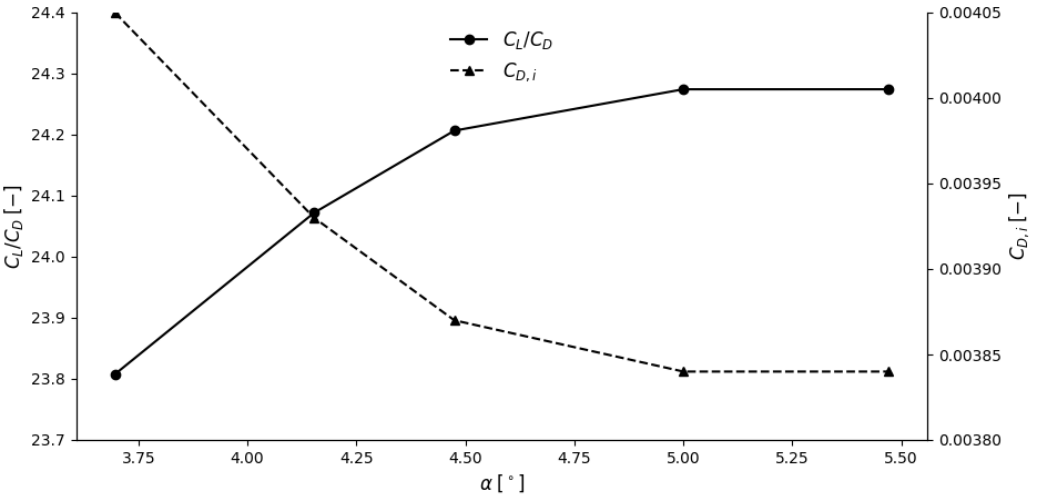

Figure 5.3: Aerodynamics efficiency and induced drag coefficient values at different angle of attack constraint values

which tends to be higher for lower imposed angle of attack constraint values. A comparable trend in twist distribution was observed by Liou et al. [35] when optimizing a blended wing body aircraft for NASA.

Table 5.3: Comparison of optimized design variables for optimizations at different α_{value} constraint values

Variable	Baseline	$\alpha_{\text{value}} = 3.8°$	$\alpha_{\text{value}} = 4.5°$	$\alpha_{\text{value}} = \text{free}$
$a_{1,\text{aft}}$ [°]	0.582	8.0	5.375	0.632
$a_{2,\text{aft}}$ [°]	-0.072	0.094	-0.045	-0.071
$a_{3,\text{aft}}$ [°]	-2.289	2.154	-0.520	-1.941
a_5 [°]	-3.000	-3.084	-3.009	-3.732
a_6 [°]	-3.813	-2.472	-1.444	-1.931
a_7 [°]	-0.941	0.342	-1.369	-0.885
a_8 [°]	-0.500	-0.966	-0.647	-0.501
Γ [°]	2.000	2.452	1.805	1.698

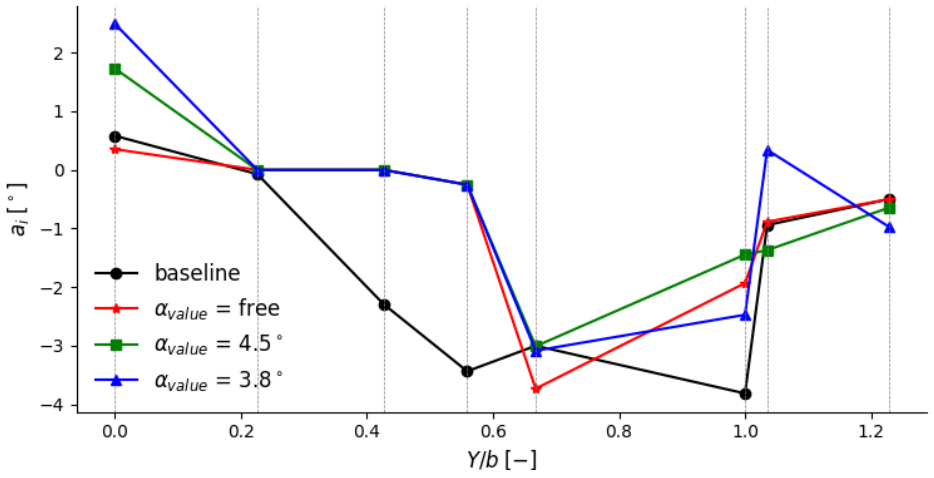

Figure 5.4: Twist distributions comparison between optimization results and baseline

5.3.1 Lift Distribution

The obtained lift distributions for each optimization case, in comparison to the baseline, are visually depicted in Figure 5.5. As illustrated in Figure 5.6, the local lift distribution is also presented. The overall shape of the resulting lift distribution exhibits characteristics reminiscent of an averaged elliptical/triangular distribution. This particular distribution pattern is recognized for achieving an optimal aerodynamic trade-off, as discussed by F. Faggiano [4] and Qin et al. [36].

Furthermore, the higher twist angle at the root section, associated with lower imposed angle of attack constraint values, is also reflected in the lift distribution. The wing root region experiences a noticeable increase in load, particularly evident for the case with $\alpha_{\text{value}} = 3.8°$, as observed in Figure 5.5. Consequently, the outboard wing region demonstrates a comparatively lower load, as depicted in Figure 5.6. Interestingly, the winglet lift and local lift distribution exhibit a similar shape across all optimization cases.

In general, the optimized lift distributions in each case exhibit higher load in the wing region between Section III and V compared to the baseline design. Simultaneously, the outboard wing region experiences a reduced load, as demonstrated by Figure 5.6. These findings highlight the effectiveness of the optimization process in redistributing the lift along the wing span to achieve improved aerodynamic performance. Additionally, it is worth noting that the highest local lift coefficient is consistently observed at the wing tip, just prior to the beginning of the winglet.

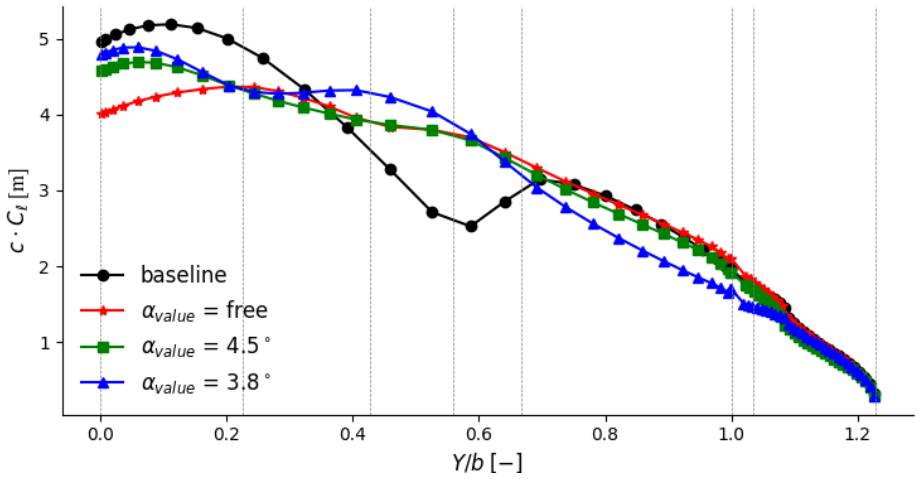

Figure 5.5: Lift distributions comparison between optimization results and baseline

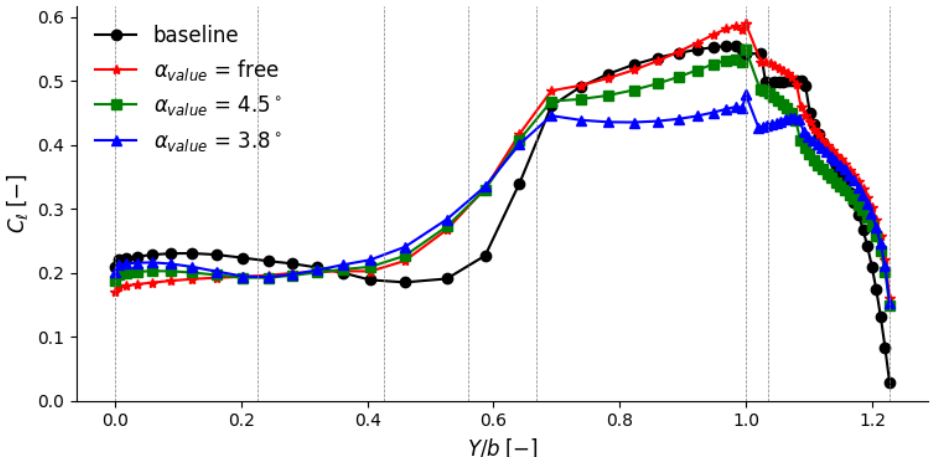

Figure 5.6: Local lift distributions comparison between optimization results and baseline

5.4 Final Design Results

As a design choice, it was decided to pursue the optimized geometry for the lowest α_{value} available. The reason behind such decision stands in the net inclination of the passenger's cabin floor during cruise. When the angle of attack is higher during cruise, it necessitates a correspondingly higher floor inclination. However, adopting such a steep inclination may present challenges or limitations in accommodating other operational conditions. Therefore, to ensure practicality and feasibility across various scenarios, a balanced approach was taken in selecting the final angle of attack. By striking a suitable compromise, the aircraft's design aims to optimize passenger comfort and safety without compromising operational requirements. Specifically, when examining the optimization results for the $\alpha_{\text{value}} = 3.8°$ scenario, it reveals an effective angle of attack of 3.7° under the considered subsonic conditions (see Table 5.4). As a result, when aiming for the same lift coefficient of 0.26 during actual cruise conditions with a higher Mach number (0.85), the resulting angle of attack becomes lower, specifically about 3.7°. This alignment satisfies the previously mentioned requirement for the passengers' cabin inclination.

As discussed in Section 3.2.2, a manual feedback loop has been implemented to refine the 3D CAD model geometry. This iterative process aims to align the CAD model as closely as possible with the optimized results obtained through the analysis. In this section, the outcomes of this refinement process will be referred to as the final design. To ensure clarity and facilitate comparison, the results will be consistently compared to both the baseline design and the reference pure optimization case $\alpha_{\text{value}} = 3.8°$, as outlined in Table 5.4.

The final design demonstrates a high level of similarity with the geometry resulting from the $\alpha_{\text{value}} = 3.8°$ optimization. However, it should be noted that it is not an exact match, which is expected due to the differing parameterization methods employed in this study. The CAD

Table 5.4: Comparison of resulting constraints and objective function for baseline, optimization results, and final design.

Case	$X_{\text{NP}} - X_{\text{CP}}$ $[m]$	α $[^\circ]$	C_{D_i} $[-]$	C_L/C_D $[-]$
Baseline	2.430	6.34	0.00458	22.7
$\alpha_{\text{value}} = 3.8^\circ$	0.434	3.70	0.00405	23.8
Final Design	0.429	3.87	0.00410	23.7

model's parameterization is more comprehensive and intricate compared to the one used in the optimization process. Consequently, the resulting values for the drag coefficient (C_{D_i}) and the lift-to-drag ratio (C_L/C_D) deviate slightly from the purely optimized values, with the former being approximately 1.2% higher and the latter being around 0.005% lower.

Despite these minor discrepancies, the achieved level of alignment was deemed satisfactory for the purposes of this study, and the *final design* serves as an acceptable outcome. The results obtained through the manual feedback loop emphasize the validity and effectiveness of the parameterized model utilized in the optimization process. Despite the significant disparity in complexity between the parameterized model and the more intricate CAD model, the adaptation of the latter yielded remarkably similar outcomes. This indicates that the simplified parameterized model can accurately represent the OML defined in the CAD model, further validating its utility and reliability in the optimization process. Thus, the study's findings not only demonstrate the success of the manual feedback loop but also reinforce the robustness of the chosen parameterization approach.

5.4.1 Final Lift Distributions

The final design lift and local lift distributions are shown in Figure 5.7 and Figure 5.8 respectively. The correspondence with the purely optimized results is almost identical, the only differences being a rather small increase in load for the final design ones around wing Section III, and a slightly lower load at the beginning of the outer wing, between Section IV and V. On the other hand, the correspondence for the winglet shows a high degree of accuracy.

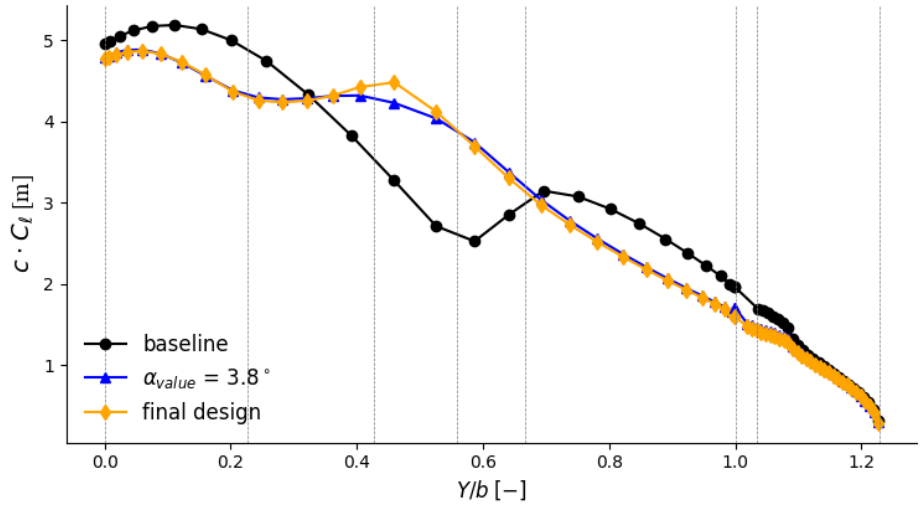

Figure 5.7: Lift distributions comparison between baseline, optimization results, and final design

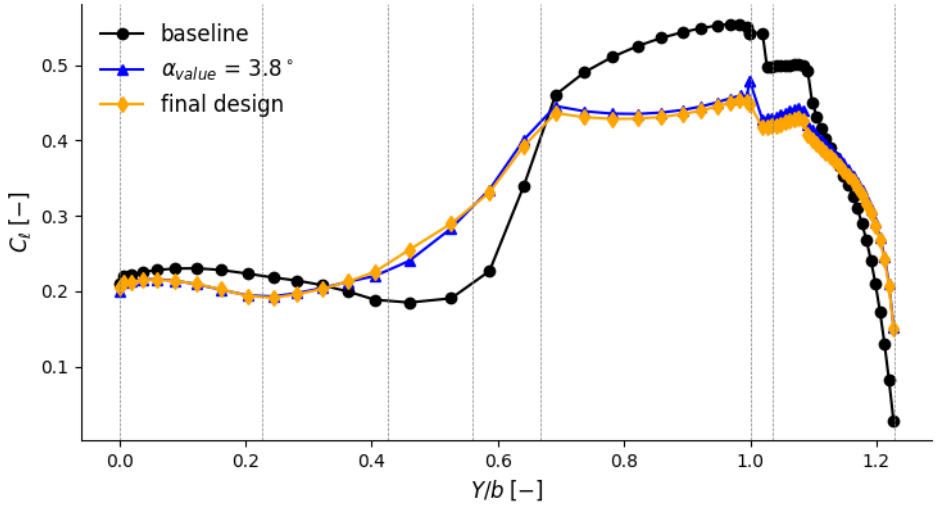

Figure 5.8: Local lift distributions comparison between baseline, optimization results, and final design

5.4.2 Local Induced Drag Distribution

In Figure Figure 5.9, the distribution of local induced drag along the wing-span is shown. Notably, the local induced drag coefficient is significantly higher near the wing root across all cases. This higher value is attributed to the presence of a larger downwash, which is a characteristic of highly swept wings. The increased downwash, in turn, leads to the generation of vortex-induced drag [21].

Moreover, it is evident that the optimized distribution of induced drag redistributes the drag production more evenly along the span of the inboard wing. Specifically, there is a slight reduction in drag between Section I and II, followed by a slight increase between Section II and IV. On the other hand, the distribution of local induced drag on the outer wing experiences a

considerable reduction.

Moving on to the final design, it exhibits an induced drag distribution that closely resembles the purely optimized geometry. However, notable differences can be observed around Section V and VI, where the trend of induced drag production is inverted, resulting in an increase towards the wing tip.

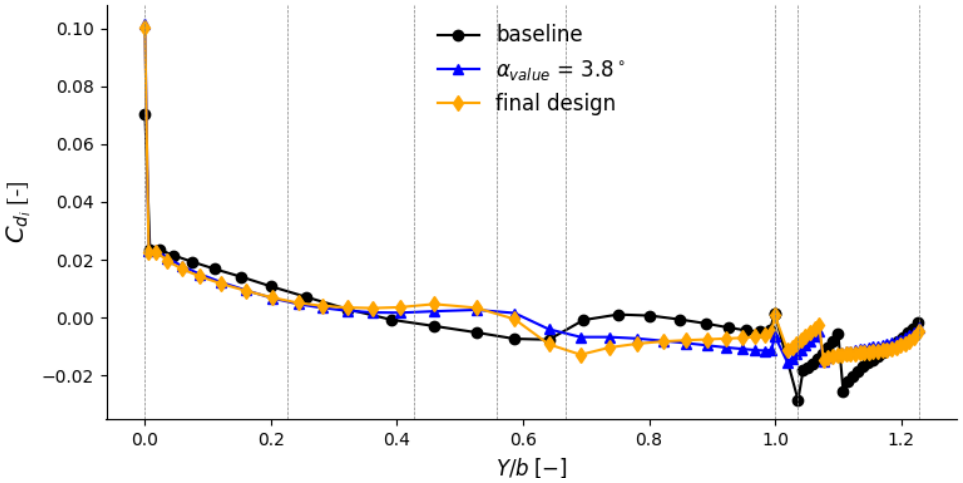

Figure 5.9: Local drag distributions comparison between optimization results, final design, and baseline

5.4.3 Inboard Wing Airfoils

As discussed in Chapter 3, the optimization process entails modifications to the inboard wing airfoils, specifically from Section I to Section IV. During this process, only the aft part of these sections is altered, while the front part remains constant to accommodate the structure of the passengers' cabin and its inclination.

Figure 5.10 displays the resulting airfoils in the specified wing region for the configuration of the final design. The modifications observed in the final design airfoils, compared to the baseline, are directly correlated to the optimized values of the design variables $a_{1,\text{aft}}$ to $a_{4,\text{aft}}$. Notably, the airfoil corresponding to Section I exhibits a drooped trailing edge, which increases the load at the wing root, as explained in the preceding text. This behavior becomes even more pronounced for Section III and Section IV, illustrated respectively as (c) and (d) in Figure 5.10, with their consequential impact on the lift distribution depicted in Figure 5.7.

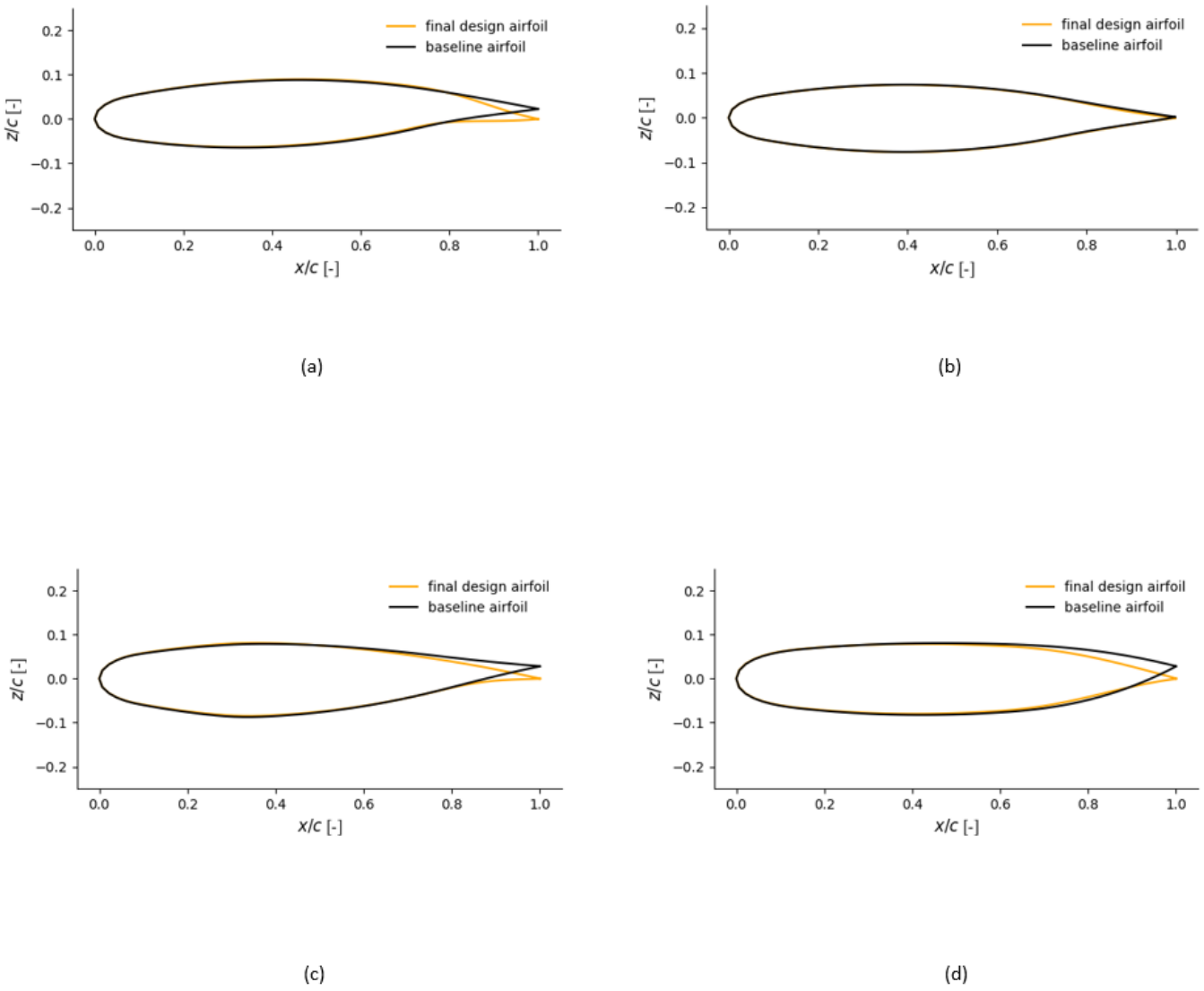

Figure 5.10: Final design vs baseline inboard wing airfoils. (a): Section I; (b) Section II; (c): Section III; (d): Section IV.

5.4.4 Drag Polar & Lift over Drag Ratio Curve

A detailed comparison between the baseline and the final design drag polar is presented in Figure 5.11a, providing valuable insights into their respective performance characteristics. The drag coefficient exhibits a significant reduction in the final design configuration across a range of lift coefficients, particularly noticeable at low C_L values leading up to the design lift coefficient. However, as the lift coefficient increases, the reduction in C_D becomes less pronounced. On the other hand, Figure 5.11b depicts the lift over drag ratio curve of the two configurations as a function of C_L. As expected, the final design exhibits a substantial increase in aerodynamic efficiency, with the highest improvement observed around the lift coefficient of 0.26 used during the optimization process. Beyond this point, the efficiency curve tends to flatten out. It is worth noting that the lift coefficient employed during the optimization process is highlighted in both figures by a dashed grey line.

When examining the curves displayed in Figure 5.11a, it becomes evident that the shape of the curves for the two configurations differs noticeably. This disparity arises due to the distinct geometric characteristics of the two designs. Notably, they feature different inboard wing airfoils, twist angles, and dihedral configurations, despite sharing a common planform shape. Consequently, their respective lift distributions at a lift coefficient of zero ($C_L = 0$) vary, explaining why the curves do not intersect at this point. While the overall net lift generated remains zero, certain sections of the wing contribute positively to lift while others generate negative lift. The circulation induced by these lift distributions introduces disturbances in the flow developing in the wake region until reaching the Trefftz plane, which is employed to calculate the induced drag. According to the relationship described in Equation 2.10, both velocity components contributing to drag generation are squared, resulting in their contribution being independent of their sign. Therefore, having different lift distributions at $C_L = 0$, the two configurations also generate two different induced drag coefficients in such conditions. This behavior is effectively captured by AVL, as depicted in Figure 5.11a, illustrating the accuracy of the model in simulating these aerodynamic phenomena.

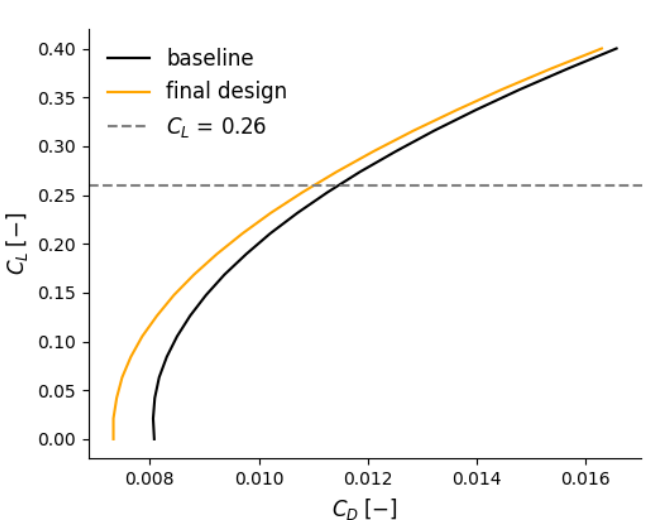

(a) Drag polar

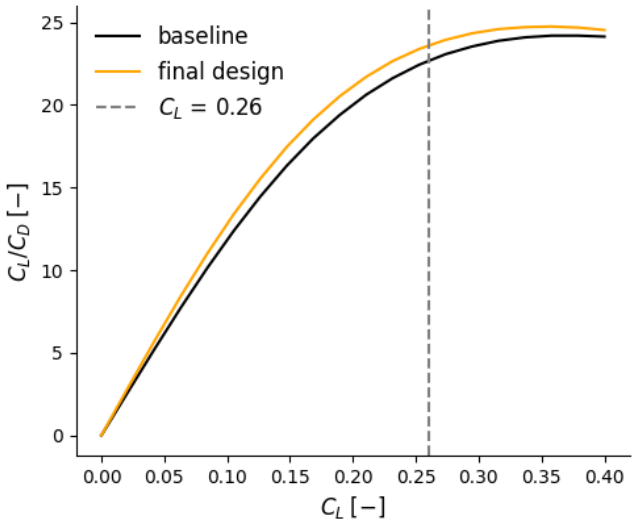

(b) Lift over drag ratio curve.

Moreover, an interesting investigation into the steepness observed in the drag polars depicted in Figure 5.11a can be made. As previously mentioned, the final design curve showcases diminished values of the drag coefficient across the entire range of lift coefficients under consideration. However, this disparity tends to level out beyond the prescribed design lift coefficient of 0.26. Given the parabolic nature of the displayed drag polars and the shared aspect ratio between the two designs, the slope of these curves is governed by the span efficiency factor e. The twist applied to the Flying V's wing gives rise to a certain level of e dependency with respect to the lift coefficient [37], as illustrated in Figure 5.12. It is worth noting that the span efficiency of

the final design consistently surpasses that of the baseline design, aligning with expectations resulting from the optimization process that yields a more elliptical lift distribution. This trend persists until a specific lift coefficient is reached, at which point the two efficiencies tend to converge to more similar values. This behavior is to be expected, as the design optimization was centered around a precise lift coefficient, thereby accentuating differences primarily around that specific point. A notable observation is the rapid increase in the enhancement of span efficiency for the final design at lower lift coefficient values, up until the designated lift coefficient of 0.26 is attained. Furthermore, it is discernible that the span efficiency exceeds unity, an outcome attributed to the presence of winglets [38]. This comprehensive analysis completes the understanding of the aforementioned drag polar curves.

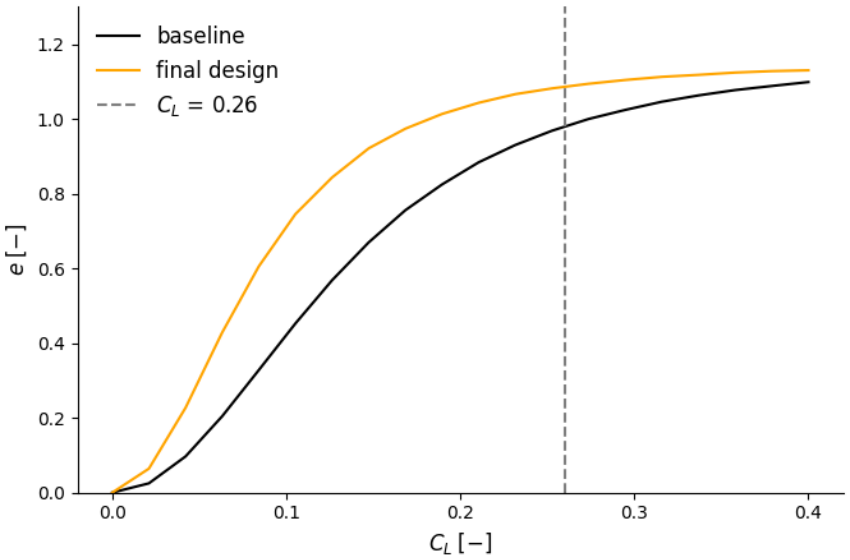

Figure 5.12: Span efficiency variation with respect to lift coefficient for baseline and final design

6

Conclusions

The objective of this study was to optimize the wing geometry of the Flying V aircraft to minimize induced drag under specific subsonic conditions ($M = 0.6$) and a given lift coefficient of 0.26. This was achieved by using a combination of the Vortex Lattice Method (VLM) and an optimization algorithm. In particular, Athena Vortex Lattice (AVL) software was employed for aerodynamics calculations, utilizing Trefftz Plane analysis to compute the induced drag.

Validation of the AVL software was conducted using experimental data from the Onera M6 wing which was chosen as a case study. Despite operating at the limit of the Prandtl-Glauert correction, the software accurately reproduced the lift distribution shape and total lift coefficient at various angles of attack.

To improve the current design of the Flying V, a simpler parameterization was introduced, to represent the complex CAD model describing the current design of the aircraft's Outer Mold Line (OML). The proposed parameterization consisted of eight sections along half the wingspan, with the first four sections representing the inboard wing region, the fifth and sixth defining the outboard wing, and the remaining sections forming the winglet geometry. The inboard wing sections were parameterized in a wire-frame style, with the front part representing the location of the passengers' cabin, requiring fixed dimensions and inclination to accommodate a suitable cabin floor. The sections' geometry was described by the inclination angles of the front and aft parts of the inboard wing sections, as well as the total incidence angle of the other sections. The design vector included the aft angles of the first three sections, the total incidence angle of the last four sections, and the dihedral of the outboard wing to ensure a straight hinge line for control power. A total of 8 design variables were utilized during the optimization process.

Two aerodynamic constraints were implemented to ensure feasible optimized results. The first constraint was related to the resulting angle of attack computed by AVL based on the defined geometry and lift coefficient input. Different values of the angle of attack constraint were investigated due to their significant impact on the final results. The second constraint required a positive distance between the aircraft's neutral point and the center of pressure, with a minimum value of 2% of the Mean Aerodynamic Chord serving as a measure of the aircraft's static margin. The optimization process utilized the COBYLA algorithm, a gradient-free and trust-region method suitable for constrained problems with unknown or computationally expensive derivatives.

A sensitivity analysis using the Morris method (Elementary Effects method) was conducted to assess the influence and interactions of each model input on the model output. The analysis revealed varying degrees of importance and variability among the variables in relation to the objective function. However, the resulting confidence intervals for the normalized mean values were relatively small, indicating a reasonable level of confidence and enhancing the reliability of the sensitivity analysis results. This approach offers a detailed and comprehensive understanding of the models behavior, aiding in decision-making, model improvement, and uncertainty reduction in complex systems such as the Flying V's wing, which can be of valuable assistance for future design changes.

Since AVL only computed induced drag, a simplified viscous module was introduced to estimate the overall lift-to-drag ratio more accurately. The profile drag was estimated using a semi-empirical strips method, accounting for approximately 50% to 60% of the total computed drag coefficients. This aligns well with existing literature, considering the simplifications made in this study, such as neglecting certain drag components like wave drag and interference drag.

Each optimization case run significantly reduced the drag coefficient compared to the initial design. Additionally, the lift distribution obtained in each run exhibited characteristics resembling an averaged elliptical/triangular distribution, which according to literature guarantees optimal aerodynamic trade-off. Overall, the optimization process successfully redistributed lift along the wing span, resulting in improved aerodynamic performance.

The optimized geometry corresponding to the lowest angle of attack constraint was chosen for further analysis considering the requirement about the inclination of the passenger's cabin floor during cruise. A manual feedback loop was implemented to refine the CAD model geometry, aligning it as closely as possible with the optimized results. Despite minor discrepancies between the purely optimized geometry and the final design, the achieved level of alignment was deemed satisfactory for this study.

The final design demonstrated improved lift-to-drag ratio and a reduction in induced drag coefficient compared to the initial design. The drag polar and lift-to-drag ratio curve comparisons confirmed the overall improvement in aerodynamic performance and the capability of AVL to capture the shape of these curves within the limits of the model. Furthermore, the results obtained through the manual feedback loop emphasized the validity and effectiveness of the parameterized model utilized in the optimization process. In particular, the final design showed a 4.38% increase in lift-to-drag ratio compared to the initial design and a 10.5% reduction in induced drag coefficient. This showcases the significant enhancements achieved in the aerodynamic performance of the optimized configuration.

Overall, this study demonstrates the successful optimization of the Flying V aircraft's wing geometry to achieve higher aerodynamic performance in terms of lift-to-drag ratio and induced drag generation in the flight conditions considered. These findings contribute to the understanding and advancement of the Flying V's wing design optimization process, paving the way for further enhancements to be obtained with future studies.

7

Recommendations

The findings of this research effort effectively showcase that the framework developed for the purpose of conducting low-fidelity aerodynamic design optimization for the Flying V's wing has successfully demonstrated its competence in achieving the intended enhancements related to induced drag reduction. However, it is important to acknowledge that the pursuit of a deeper exploration of the design space due to the preliminary nature of the design phase, combined with a consequent need for a faster optimization process, necessitated the incorporation of a simplified parametric model. While this pragmatic approach indeed expedited the optimization and showed a good level of accuracy, it also introduced certain simplifications that require a more thorough investigation and potential avenues for refinement, thereby setting the stage for subsequent research endeavors.

A critical consideration in this context pertains to the validation of the outcomes stemming from the optimized design, using higher-order methodologies such as CFD. The application of these techniques holds particular significance in assessing the lift distribution across the wing span, providing valuable insights into the reduction of induced drag at the flight conditions under examination. This analysis would shed light on the intricacies of the flow behavior in transonic regimes, with a specific focus on the thicker sections of the wing structure. In these regions, the development of the boundary layer may lead to an increased perceived thickness experienced by the airflow, subsequently influencing the local production of the lift and, consequently, exerting an effect on induced drag.

Moreover, an added margin of improvement can be pursued for the optimized design attained in this present study, employing the higher-order methodologies mentioned above such as CFD.

The resultant design itself can serve as a foundational point of departure for a more refined and accurate design optimization process. This subsequent phase could directly manipulate the aircraft's OML contour obtained with the present study and its parameterization in the CAD environment, avoiding the necessity of incorporating simplified parameterized models. This shift also includes the integration of the actual profiles and dimensions characterizing each individual wing section of the Flying V, including their inherent thickness. This is currently being investigated by other contributors to the project.

References

[1] ICAO. *Future of Aviation*. 2023. URL: https://www.icao.int/Meetings/FutureOfAviation/Pages/default.aspx.

[2] United Nations Development Program (UNDP). *Sustainable Development Goals*. 2023. URL: https://www.undp.org/sustainable-development-goals.

[3] Nadir Yilmaz and Alpaslan Atmanli. "Sustainable alternative fuels in aviation". In: *Energy* 140 (2017), pp. 1378–1386.

[4] Francesco Faggiano et al. "Aerodynamic design of a flying V aircraft". In: *17th AIAA Aviation Technology, Integration, and Operations Conference*. 2017, p. 3589.

[5] S. Chernyshev, Sergey Lyapunov, and Andrey Wolkov. "Modern problems of aircraft aerodynamics". In: *Advances in Aerodynamics* 1 (Dec. 2019). DOI: 10.1186/s42774-019-0007-6.

[6] Justus Benad. *The Flying V a new aircraft configuration for commercial passenger transport*. 1st ed. Bonn: Lilienthal Oberth e.V., 2015.

[7] Alberto Ruiz Garcia, Roelof Vos, and Coen de Visser. "Aerodynamic model identification of the flying V from wind tunnel data". In: *AIAA Aviation 2020 Forum*. 2020, p. 2739.

[8] Marco Palermo and Roelof Vos. "Experimental aerodynamic analysis of a 4.6%-scale flying-v subsonic transport". In: *AIAA Scitech 2020 Forum*. 2020, p. 2228.

[9] T. Cappuyns. *Handling Qualities of a Flying V Configuration*. Delft: MSc's Thesis, TU Delft Aerospace Engineering, 2019.

[10] Marleen Hillen. *Parametrisation of the Flying-V Outer Mould Line*. Delft: MSc's Thesis, TU Delft Aerospace Engineering, 2020.

[11] Nikki Van Luijk. *Constrained Aerodynamic Shape Optimisation of the Flying V Outer Wing*. Delft: MSc's Thesis, TU Delft Aerospace Engineering, 2023.

[12] Justus Benad and Roelof Vos. "Aerial vehicle, Patent application N2034242". In: (2023).

[13] John Anderson. *Fundamentals of Aerodynamics*. McGraw Hill, 2011.

[14] Snorri Gudmundsson. *General Aviation Aircraft Design: Applied Methods and Procedures*. Butterworth-Heinemann, 2014.

[15] H von Helmholtz. "Über Integrale der hydrodynamischen Gleichungen, welche den Wirbelbewegungen entsprechen." In: (1858).

[16] I. M. Kroo. “DRAG DUE TO LIFT: Concepts for Prediction and Reduction”. In: *Annual Review of Fluid Mechanics* 33 (2001), pp. 587–617.

[17] Stephen C Smith. *A computational and experimental study of nonlinear aspects of induced drag*. Tech. rep. 1996.

[18] M. Drela and H. Youngren. *AVL*. 2022. URL: http://web.mit.edu/drela/Public/web/avl/.

[19] Guido Van Rossum and Fred L. Drake. *Python 3 Reference Manual*. Scotts Valley, CA: CreateSpace, 2009. ISBN: 1441412697.

[20] *AVLWrapper*. 2023. URL: https://pypi.org/project/avlwrapper/.

[21] Francesco Faggiano. *Aerodynamic Design Optimization of a Flying V Aircraft*. Delft: TU Delft Aerospace Engineering, 2016.

[22] John P Campbell and Marion O McKinney. *Summary of methods for calculating dynamic lateral stability and response and for estimating lateral stability derivatives*. Tech. rep. 1951.

[23] Michael JD Powell. “A view of algorithms for optimization without derivatives”. In: *Mathematics Today-Bulletin of the Institute of Mathematics and its Applications* 43.5 (2007), pp. 170–174.

[24] *scipy.optimize Function*. 2008-2023. URL: https://docs.scipy.org/doc/scipy/tutorial/optimize.html.

[25] Pauli Virtanen et al. “SciPy 1.0: Fundamental Algorithms for Scientific Computing in Python”. In: *Nature Methods* 17 (2020), pp. 261–272. DOI: 10.1038/s41592-019-0686-2.

[26] E. Torenbeek. *Blended-wing-body aircraft: A historical perspective*. In R. Blockley, Shyy (Eds.) Encyclopedia of Aerospace Engineering John Wiley, and Sons, 2016.

[27] Ohad Gur, William H Mason, and Joseph A Schetz. “Full-configuration drag estimation”. In: *Journal of Aircraft* 47.4 (2010), pp. 1356–1367.

[28] Daniel Raymer. *Aircraft design: a conceptual approach*. American Institute of Aeronautics and Astronautics, Inc., 2012.

[29] Andrea Saltelli et al. *Global sensitivity analysis: the primer*. John Wiley & Sons, 2008.

[30] Herman Jon and Usher Will. *SALib - Sensitivity Analysis Library in Python*. 2023. URL: https://salib.readthedocs.io/en/latest/.

[31] V. Schmitt and F. Charpin. “Pressure Distributions on the ONERA-M6 wing at transonic Mach numbers”. In: *AGARD Advisory Report No. 138 - Experimental Data Base for Computer Program Assessment* 1 (1979), B1–1 –B1–44.

[32] J.W. Slater. *ONERA M6 WING*. 2021. URL: https://www.grc.nasa.gov/www/wind/valid/m6wing/m6wing.html.

[33] Lewis R Fisher. *Approximate corrections for the effects of compressibility on the subsonic stability derivatives of swept wings*. 1854. National Advisory Committee for Aeronautics, 1949.

[34] Erwin Gowree. *Influence of Attachment Line Flow on Form Drag*. Doctoral thesis, City University London, 2014.

[35] M-F Liou et al. "Aerodynamic design of integrated propulsion–airframe configuration of a hybrid wing body aircraft". In: *Shock Waves* 29.8 (2019), pp. 1043–1064.

[36] Ning Qin et al. "Aerodynamic considerations of blended wing body aircraft". In: *Progress in Aerospace Sciences* 40.6 (2004), pp. 321–343.

[37] Lance Traub. "Calculation of the Oswald Efficiency Factor from Drag Polars: A Critical Assessment". In: *Journal of Aircraft* 59 (July 2022), pp. 1–8. DOI: 10.2514/1.C036886.

[38] John H McMasters et al. *Advanced configurations for very large subsonic Transport Airplanes*. Tech. rep. 1996.